Nanoscale

ROYAL SOCIETY OF CHEMISTRY

PAPER

View Article Online
View Journal | View Issue

Cite this: *Nanoscale*, 2025, **17**, 1616

Tough, durable and strongly bonded self-healing cartilage-mimicking noncovalently assembled hydrogel nanostructures: the interplay between experiment and theory†

Shikha Awasthi, *[a] Sarvesh Kumar Pandey, *[b] Hulikere Jagdish Shwetha,[c] Nehal[a] and S. Selvaraj[d]

High-strength, strongly bonded and self-healing materials are of great interest for several applications; however, the experimental and *in silico* design of all such properties in a single material is challenging. In the present work, inspired by cartilage tissue, polyacrylamide (PAM)-based tough and durable dimer (PAM-Ag and PAM-BNOH) and trimer (PAM-Ag-BNOH) nanocomposites were synthesized by encapsulating silver (Ag) and hydroxylated hexagonal boron nitride (BNOH). Strong interfacial interaction was achieved by introducing (computational modelling and DFT approaches) noncovalent bonds in the dimer and trimer nanohybrids. The fabricated PAM-Ag-BN nanocomposite showed higher mechanical strength (0.31 MPa compressive strength and 0.29 MPa Young's modulus) than dimer hydrogel composites. The long-term durability of the hydrogel samples was tested by electrochemical testing of hydrogels in a simulated body fluid, and a higher corrosion resistance (i_{corr} = 2.65 × 10^{-5} A cm^{-2}) was obtained for trimer hydrogels. Moreover, the supramolecular cross-linked assembly of PAM-Ag-BN perfectly exhibited bioactivities, including bone formation ability, self-healing performance, restricted cytotoxicity, and antimicrobial activity. The synergistic effect of nano- and micron-sized particles in PAM-Ag-BN ensued in strong interfacial interlocking through the formation of hydrogen bonding between Ag, BNOH and PAM. Therefore, the fabricated tough hydrogel composite can be a leading biomaterial for soft tissue (articular cartilage) regeneration. The present research opens new directions for developing smart self-healing nanocomposites, which are extensively used in cartilage tissue engineering.

Received 12th August 2024,
Accepted 20th November 2024

DOI: 10.1039/d4nr03322a

rsc.li/nanoscale

1. Introduction

Soft materials have tremendous applications in industrial, biomedical and engineering fields.[1–3] The structure of the semi-solid soft hydrogel resembles that of the articular cartilage tissue, having a three-dimensional structure with an excess amount of water.[4–7] The articular cartilage remains as a thin layer and covers mainly the surface of joints. The normal and healthy joints of articular cartilage are termed hyaline articular cartilages. The articular cartilage majorly provides lubrication

[a]*Department of Chemistry, School of Basic Sciences, Manipal University Jaipur, Jaipur – 303007, Rajasthan, India. E-mail: awas.shikha2212@gmail.com, sarvesh@manit.ac.in*
[b]*Department of Chemistry, Maulana Azad National Institute of Technology, Bhopal – 462003, Madhya Pradesh, India*
[c]*Department of Materials Engineering, Indian Institute of Science Bengaluru, Bengaluru – 560012, Karnataka, India*
[d]*Department of Physics, Saveetha School of Engineering, Saveetha Institute of Medical and Technical Sciences, Thandalam, Chennai – 602105, Tamil Nadu, India*

† Electronic supplementary information (ESI) available: Fig. S1: Preparation of hydrogel for electrochemical testing. Fig. S2A: (i) SEM image, (ii) XRD pattern and (iii) elemental mapping of the PAM-Ag-BN trimer composite showing (a) surface morphology, (b) elemental B distribution, (c) elemental C distribution, (d) elemental N distribution, (e) elemental O distribution, (f) elemental Ag distribution and (g) EDS. Fig. S2B: Images of the self-healed sample: (a) two halves of the PAM-Ag-BN sample, (b) self-healing of the sample and (c) force applied on the self-healed sample, showing a significant recovery. Fig. S3: QTAIM-based molecular graph of the Ag assembly as a component model. Fig. S4: QTAIM-based molecular graph for the PAM monomer unit chosen as a model. Fig. S5. QTAIM-based molecular graph for the BNOH monomer unit chosen as a model. Fig. S6. QTAIM-based molecular graph for the PAM-BNOH composite model. Fig. S7. QTAIM-based molecular graph for the PAM-Ag composite model. Fig. S8. QTAIM-based molecular graph for the PAM-Ag-BNOH composite model. Table S1. Some important and selected QTAIM-based topological parameters [ρ, $\nabla^2(\rho)$, V, DI (A, B)] of the PAM parent (monomer) unit. Table S2. Some important and selected QTAIM-based topological parameters [ρ, $\nabla^2(\rho)$, V, DI (A, B)] of the BNOH parent (monomer) unit. Table S3. Some important and selected QTAIM-based topological parameters [ρ, $\nabla^2(\rho)$, V, DI (A, B)] of the PAM-BNOH composite model. Table S4. Some important and selected QTAIM-based topological parameters [ρ, $\nabla^2(\rho)$, V, DI (A, B)] of the PAM-Ag composite model. Table S5. Some important and selected QTAIM-based topological parameters [ρ, $\nabla^2(\rho)$, V, DI (A, B)] of the PAM-Ag-BNOH composite model. See DOI: https://doi.org/10.1039/d4nr03322a

to the joints for better functioning, but the presence of lesions can damage the active joints and cause osteoarthritis.[8] Severe damages are cured by surgeries, while mild damages in cartilage tissues can be treated by physiotherapy, which offers strength to the nearby muscles. The replacement of cartilage with an artificial scaffold using hydrogels has a restricted endurance due to its poor mechanical and load-bearing strength, and it requires re-surgeries in young-aged patients after the implantation of the cartilage scaffolds. Thus, there is an essential requirement for a functional, appropriate and durable implant material for the alleviation of post-surgical complications.[9,10] The hydrogels can be classified as natural (collagen, fibrin, alginate, chitosan, and gelatin) and synthetic hydrogels (polyvinyl alcohol, polyethylene glycol, polyacrylamide, and polyanhydrides), which are used for the construction of cartilage implants.

Synthetic polyacrylamide (PAM) hydrogels are made up of acrylamide subunits and prepared majorly by a cross-linking method. There are three methods for the preparation of hydrogels, namely, radiation method, cross-linking method and free radical polymerization method.[11–15] The restricted strength of the polyacrylamide hydrogels was altered by several researchers using different synthesis methods or different reinforcing agents. Shi-Neng Li *et al.*[16] used a cross-linking method to prepare PAM/chitosan hydrogels. The hydrogel was cross-linked by hyperbranched polysiloxane (HSi). The fabricated composite hydrogel exhibited improved mechanical strength (with 302 kPa tensile strength, 2263% elongation break and 3.85 MJ m^{-3} of toughness) due to the strong interaction between the network of matrix and additives. The researchers are using various fabrication techniques as well as several reinforcing agents in PAM to mitigate the appalling concerns of the hydrogels. However, among all, the cross-linking method for the preparation of PAM hydrogel is of great interest.[17] The reinforcing additives play a very crucial role in the advancement of the hydrogel properties by strengthening the interfacial bonding between the matrix and reinforcements. The reinforcing agents, which are being used in biomedical applications, must be biocompatible, for example, silver, titanium oxide, hexagonal boron nitride, carbon nanotubes (CNTs), and silicon oxide. Silver (Ag) nanoparticles display impactful antimicrobial activities along with anti-inflammatory and antiangiogenic properties,[18–21] and therefore, they are nanomaterials of high demand for diagnostic and therapeutic applications. For, cartilage applications, Olăreț *et al.*[22] synthesized polyacrylamide hydrogels grafted with Ag-decorated CNT nanoparticles. The addition of Ag-decorated CNT reduced the hysteresis (from 13.25 to 7.65) and enhanced the compression stress (up to 630 kPa) for all the composites. The composite hydrogels further showed a noteworthy antibacterial activity when tested against Gram-positive (*S. aureus*) and Gram-negative bacteria (*E. coli*). The superior antimicrobial activity (98%) of hydrogel composites was observed with Gram-positive bacteria over Gram-negative bacteria (95%). Thus, it was established by this study that the addition of Ag-decorated CNTs in the PAM matrix resulted in high mechanical strength and antibacterial activity, which may have potential application in bone tissue regeneration. Though silver-added PAM hydrogel composites are rarely reported in the literature, Isabel González-Sánchez[23] and co-workers reported methacrylate hydrogels with Ag nanoparticles for tissue engineering. The cross-linking was used to integrate silver nanoparticles in the methacrylate hydrogels with antimicrobial activities. Furthermore, the addition of boron nitride (BN) in the hydrogel matrix may alter the strength of materials.[24–27] For instance, Xue *et al.*[28] reported enhanced strength and self-healing performance of functionalized boron nitride nanosheet (BNNS)-added hydrogel composites. The BNNS was modified by using the NH_2 group and BNNS-NH_2 was further reinforced in poly(acrylic acid) hydrogels (PAA/BNNS-NH_2). The concentration of BNNS-NH_2 was varied as 0.1, 0.5, 0.8 and 1.0 mg l^{-1}. Among all, 0.5 mg l^{-1} concentration exhibited improved mechanical properties such as 1311 kPa fracture stress and 4.7 MJ m^{-3} along with perfect self-healing behaviour due to the hydrogen bonding and metal coordination interactions. The better performance of hexagonal boron nitride (hBN) over graphene oxide was also observed by Duan *et al.*[29] in the polyacrylamide matrix. The compressive strength was reported to be maximum (600 kPa) for 0.12 wt% of hBN content in PAM. This enhancement by the addition of hBN in PAM was suggested due to strong interfacial interactions.

Thus, herein, varying concentrations of Ag (PAM-Ag) and BNOH (PAM-BN) in the PAM matrix were used to create the new hydrogel composites, both individually and in combination (PAM-Ag-BN). The optimum content was observed to be 0.1 and 0.3 wt% for Ag and BNOH respectively, which were shown to be more hydrophilic with the least degradation due to the thick and compact network of composite polymers by encapsulating nanoparticles. The hydrophilicity, swelling behaviour, and degradation of hydrogels were compared. A crucial feature to look into is the hydrogels' durability while examining interior tissue damage. The electrochemical approach in the simulated body fluid can be used to study this hydrogel behaviour. This method might be used to assess the damage of cartilage implants in body fluid after long-term use. The electrochemical approach has not yet been thoroughly investigated for hydrogels, despite the fact that it can yield highly important information for soft materials. Thus, the electrochemical stability of the prepared hydrogel composites is reported herein for the first time for the cartilage applications. Having a subtle glance and better understanding of the possible structural features, stability/energetics, and electronic properties of the proposed composite model, the computational modelling approach including quantum chemical calculations tools (QCCs) is one of the best alternatives which facilitates significant information about the aforementioned features. The significant advantage of performing theoretical studies is that the molecular modelling approach and QCCs can provide relevant information about the atomic interactions between the constituent components playing imperative roles

in stabilizing any particular composites, for example, the interfacial interactions (like metal-nonmetal, weak to moderate to strong hydrogen bond and vdW interactions) between the interacting atoms of two constituent component models (PAM, Ag, and BNOH). Such tools provide not only a clue about the interfacial interaction features but also the type, nature, and strength of interactions involved in the given configurations of the assembled composite models. Therefore, three theoretical composite models (PAM-Ag, PAM-BN, and PAM-Ag-BN) were adopted in this research work and an extensive computational experiment was conducted to gain some new insights into the H-bonding, other noncovalent interaction(s) (NCIs), and van der Waals (vdW)-type interactions in the combination of the prepared hydrogel PAM associated with Ag and BNOH. The present investigations revealed that the combination of Ag and BNOH in PAM, having noteworthy mechanical strength, durability and bioactivity, can be a potential hydrogel composite for cartilage repair.

2. Materials and methods

2.1. Experimental studies

2.1.1. Synthesis of Ag nanoparticles, functionalization of hBN and preparation of dimer hydrogel composites. The free radical polymerization reaction was used to synthesize polyacrylamide hydrogel (PAM). The monomer was acrylamide (10 g) while the catalysts were ammonium persulfate (0.20 g) and tetramethylethylenediamine (610.14 μl). *N*,*N*′-Methylene bisacrylamide (0.266 g) was introduced as a crosslinker during the cross-linking reaction.[30] All chemicals were procured from Sigma-Aldrich. The Ag nanoparticles were synthesized from $AgNO_3$ using a conventional chemical process.[31] Then 30 mL of 0.002 M sodium borohydride ($NaBH_4$) solution was taken in a flask (in an ice bath) with continuous stirring. The ice bath reduces the rate of decomposition of sodium borohydride during the chemical reaction. The solution of $AgNO_3$ (2 mL of 0.001 M) was introduced drop-wise into the stirred mixture followed by the addition of a few drops of NaCl, which turned the suspension yellowish to grey-coloured. A polymeric compound, poly(vinylpyrrolidone), was used as a protective agent for the stabilization of Ag nanoparticles. The Ag nanoparticles (~30–50 nm) were obtained after filtering and drying the resulting precipitate. The hydrophilicity of hBN was improved by the functionalization of hBN with the –OH group (hydroxylated boron nitride, BNOH), for which, 3 g of hBN was immersed in 12 ml of concentrated H_2SO_4, 2.5 g of $K_2S_2O_8$ and 2.5 g of P_2O_5 at 80 °C with continuous stirring for 5 h.[32] The solution was then cooled at room temperature followed by the dilution of the solution with 500 ml of deionized water. The mixture was then filtered, washed and added to 120 ml of concentrated H_2SO_4 on an ice bath. After that, 15 g of $KMnO_4$ was added with vigorous stirring for the oxidation reaction. The mixture was heated at 35 °C with stirring for 2 h and 250 ml of deionized water was introduced slowly along with the stirring for the next 2 h. The termination of the reaction was caused by mixing the 700 ml of water and 20 ml of 30 wt% H_2O_2. The white-coloured mixture was filtered, washed and dried at 60 °C. Finally, the hydroxylated boron nitride was obtained with better hydrophilicity for biomedical applications. The surface morphology of the Ag nanoparticles, hBN and as-prepared BNOH powder is given in Fig. 1. The spherical-shaped Ag nanoparticles with ~30–50 nm size can be observed in Fig. 1a. Similar surface morphology and size were also reported by Yin *et al.* for Ag nanoparticles.[33] When exposed to an SEM electron beam, the as-prepared OH-BNNS, which are made up of aggregations of thin, folded nanosheets, becomes flakier and transparent in comparison to the initial BN powder (Fig. 1a and b). Similar images of hBN and BNOH were reported by Jing *et al.*[34] Furthermore, the reinforcement of Ag and BNOH (~1 μm in size) was done by preparing the aqueous solution of different concentrations of Ag (0.1, 0.3 and 0.5 wt%) and BNOH (0.1, 0.3 and 0.5 wt%) and immersing the dried mass of neat PAM hydrogel separately in the solutions. The extra bounded ions from the surface of PAM hydrogel composites were removed by immersing the dimer composites in deionized water for 1 day. Thus, based on the Ag and BNOH concentration, six dimer composite hydrogels were prepared as PAM-Ag1 (0.1 wt% Ag), PAM-Ag3 (0.3 wt% Ag), PAM-Ag5 (0.5 wt% Ag), PAM-BN1 (0.1 wt% BNOH), PAM-BN3 (0.3 wt% BNOH), and PAM-BN5 (0.5 wt% BNOH). The optimum concentration of Ag and BNOH was used to prepare a trimer composite hydrogel for further investigations. The details of the optimum concentrations, preparation and characterization of trimer hydrogels are described in subsequent sections of the paper.

2.1.2. Physiochemical characterizations of dimer hydrogels. The morphology of the prepared samples was analysed by elemental mapping and energy-dispersive spectroscopy using the cross sections of samples under a scanning electron microscope (FE-SEM model Ultra 55 Karl Zeiss). The retention of phases after sample preparation was confirmed using an X-ray diffractometer (Rigaku SmartLab) with λ = 1.5417 Å Cu-Kα wavelength. A scan rate of 3° min^{-1} and a scan step size of 0.02° were utilized along with 2θ range from 20 to 80°. After the observation of morphology and phases, the presence of functional groups was verified by Fourier transform infrared (FTIR) spectroscopy in the range of 500–4000 cm^{-1} wave numbers.

2.1.3. Hydrophilicity, swelling and degradation of hydrogel composites *in vitro*. The hydrophilicity of the dimer samples was evinced by contact angle (Dataphysics TC/TEC 400) measurement. The angle formed between the fluid drop and the surface of the hydrogel displayed the contact angle. The phosphate buffered saline (PBS, pH 7.4) fluid with 5 μl drop was used for the identification of the hydrophilicity of biomaterials. The contact angle values were interconnected with surface roughness values obtained by atomic force microscopy (Bruker Dimension ICON AFM). The samples were scanned in lift mode (100 nm lift) with a 20 μm scan size.

The swelling characteristic of dimer hydrogel composites was calculated by drying the hydrogel samples and the dried

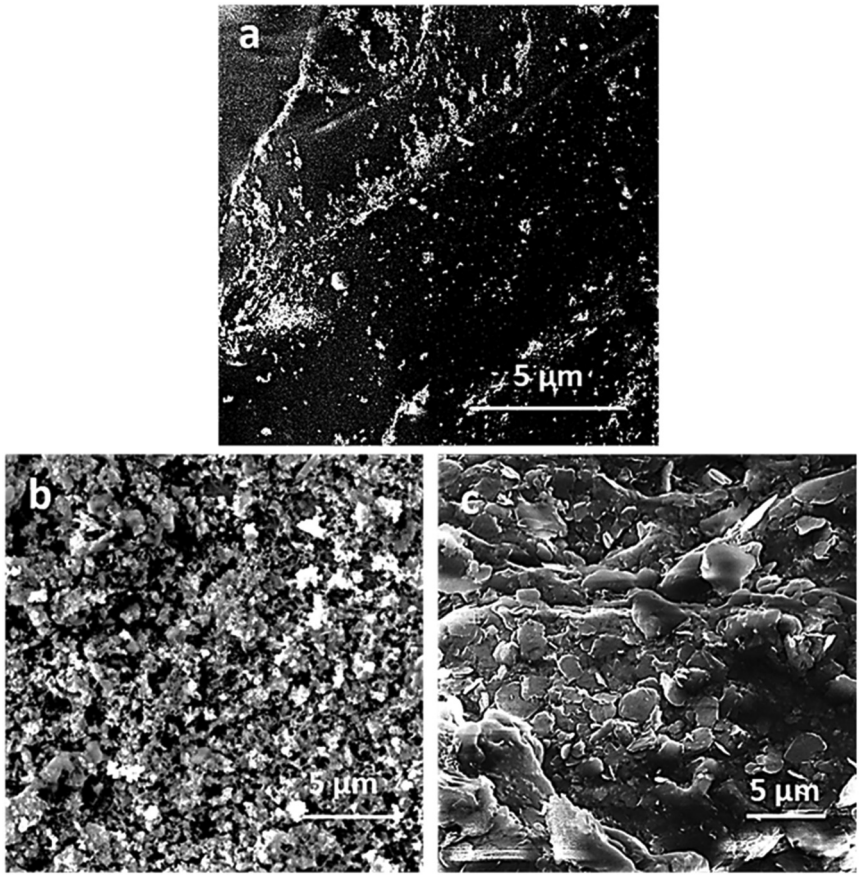

Fig. 1 Scanning electron microscopic images of (a) Ag nanoparticles, (b) hBN powder and (c) as-prepared BNOH.

mass of all samples (PAM-Ag1, PAM-Ag3, PAM-Ag5, PAM-BN1, PAM-BN3, and PAM-BN5) were weighed initially and then immersed in 100 ml of PBS (having pH 7.4) at 37 °C for 1 day. The swelling reached at its equilibrium after 24 h and the engorged samples were weighed at different time durations of 2 h, 5 h, 10 h, 15 h, 20 h and 25 h. The following equation was used to calculate the swelling ratio (SR):

$$\mathrm{SR} = \frac{W_s - W_i}{W_i} \quad (1)$$

where W_s is the weight of the hydrogel at equilibrium swelling, where equilibrium swelling elucidates maximum swelling that occurs after a particular time interval. For example, the final weight measured for the immersed dried hydrogel samples after 2 h was equilibrium swelling for 2 h (same process for all time intervals given in Fig. 6a), and W_i is the weight of the hydrogel at the initial state (weight of dried hydrogel samples). The degradation performance of samples was measured after 48 h of immersion in PBS as the samples started wrecking after 48 h in PBS. The samples were taken out from PBS after 48 h and the mass was noted for all the samples. The hydrogel samples were again dipped in PBS for degradation and the residual mass was recorded at various time intervals of 0–20 days. The remaining mass (%) of the samples was calculated using the following equation:

$$\text{Remaining gel}(\%) = \frac{W_0 - W_t}{W_0} \times 100 \quad (2)$$

where W_0 is the weight of hydrogel after 48 hours and W_t is the weight of hydrogel after time t. The mean results of the triplicate measurements were presented in the experimental data.

2.1.4. Compression test. The mechanical strength of the samples was checked by a compression test. The 10 mm × 10 mm dimension of the samples was used for the compression testing using a universal machine (Magnum Pvt. Ltd, India). A 3.33 mm min^{-1} constant rate of compression was used for the compression testing. Based on the performance in the compression test, further studies were executed on three samples, for example, one PAM-Ag-based dimer sample, one PAM-BN-based sample (having the highest compressive strength) and one trimer composite sample.

2.1.4. Preparation of the trimer composite and its characterizations. The trimer composite was synthesized based on the hydrophilicity, degradation and compressive strength of the dimer composites. The optimum concentrations of Ag and BNOH were decided between 0.1 wt%, 0.3 wt% and 0.5 wt%.

The dried mass of neat PAM hydrogel was immersed in the mixture of obtained ideal content of Ag and BNOH for 24 h. After that, the sample was washed and again immersed in deionized water to eradicate non-bonded or extra-bonded ions. Thus, the trimer hydrogel composite (PAM-Ag1-BN3) was further investigated for surface morphology (using SEM), phases (using XRD), and compression test. Moreover, the cyclic loading, needle insertion test, and tribological investigations on the current samples (PAM-Ag1, PAM-BN3 and PAM-Ag-BN) are under process as extended work of the current article (mechanical and tribological performance of silver and hydroxylated boron nitride-encapsulated polyacrylamide hydrogels, unpublished work).

2.1.5. Characterization of long-term stability of samples by electrochemical investigations. In order to check the long-term stability of prepared implants in body fluid, three hydrogel samples (two dimer samples with the optimum concentration of Ag and BNOH and one trimer sample) were tested for electrochemical performance in SBF using an electrochemical workstation (CHI 604E). For this purpose, the treatment of hydrogel samples was done and the samples were cut and the sections of hydrogels were transferred to a metal alloy surface (presented in Fig. S1†).[35] The four types of samples were prepared for the testing as PAM (bare PAM was used for electrochemical testing only because the corrosion performance of PAM was evaluated for the first time here), PAM-Ag1, PAM-BN3 and PAM-Ag-BN on the titanium alloy surface. The extrapolation of potentiodynamic polarization curves was done for the calculations of the corrosion rate. An electrochemical setup with three electrodes was used, in which a platinum foil was used as the counter electrode and saturated Ag/AgCl as the reference electrode. Open circuit potential (OCP) was stabilized for all the samples. Subsequently, potentiodynamic polarization was done in the potential range from ±200 mV at a scan rate of 0.1 mV s^{-1} from OCP. The SEM was used to observe the destruction of the material's surface after corrosion.

2.1.6. Apatite formation and self-healing of hydrogel composites. The growth of apatite crystals (biomineralization/bone-forming ability) on the surface of materials also parades the bioactivity of the implant materials. The biomaterials are generally itemised by their ability of nucleation as well as the proliferation of apatite (calcium phosphate crystals), which can persuade calcification. The development of apatite crystals on the surface of hydrogels takes place in two stages:[36] first, calcium and phosphate were added on the hydrogel in SBF until the super-saturation was achieved. Afterwards, from the super-saturated fluid, the apatite crystals deposited on the hydrogel surface. For this purpose, the samples were immersed in SBF for 48 hours at 37 °C. The confirmation of the formation of apatite crystals on the surface of hydrogel composites was done by using SEM and XRD. The self-healing of any implant material is a crucial behaviour to recover itself in body fluid after any damage. This important phenomenon of the sample was observed by cutting the trimer composite in two halves and kept in a Petri dish. The two parts of the sample were placed together and a few drops of deionized water were dispersed on the broken surface. The sample was left untouched for 24 h. The force was applied by hands on the healed sample to test the noteworthy recovery followed by the compression test.

2.1.7. Characterization of biocompatibility of the samples

2.1.7.1. Cytotoxicity assessment on chondrocyte cells. The cytotoxicity of PAM-Ag1, PAM-BN3 and PAM-Ag-BN was tested using human chondrocyte C28/I2 cell lines. In brief, UV-sterilized hydrogel samples were soaked separately in serum-free media for 24 h in a 6-well plate at 37 °C. After incubation, the supernatant (conditioned media) was collected and filtered using a 0.22 μM filter. This conditioned media was stored at 4 °C for cell treatment. The chondrocyte C28/I2 cells (Passage-22) were procured from the American Type Culture Collection (ATCC®) (Manassas, Virginia, USA) and cultured using Dulbecco's Modified Eagle's Medium (DMEM/F-12) supplemented with 10% FBS, 1% penicillin, and streptomycin and incubated at 37 °C in 5% CO_2 and 80–90% humidity. C28/I2 cells (5×10^4 per well) were seeded in a 96-well plate and incubated for 24 h; after that 100 μl of conditioned media (changed alternative day) were supplemented and incubated for 3, 5 and 7 days. The percentage of cell viability was measured by an MTT assay 3-(4,5-dimethylthiazol-2-yl)-2,5-diphenyl tetrazolium bromide on 3, 5 and 7 days. Briefly, on respective days, 20 μl of MTT reagent (0.5 mg mL^{-1}) was added to wells and incubated for 3 h. Media was removed and 100 μl of DMSO was added to solubilize the MTT formazan and read at 570 nm using a microplate reader. After removing the MTT reagent, 100 μL of DMSO was added, and the media's optical density (OD) was measured at 570 nm to determine the cell viability:

$$\text{Cell viability}(\%) = \frac{OD_{test} - OD_{blank}}{OD_{control} - OD_{blank}} \times 100 \quad (3)$$

where the optical densities of cells incubated with hydrogels, just medium without cells, and media with cells are, respectively, represented by the variables OD_{test}, OD_{blank} and $OD_{control}$. Additionally, the OD values at 570 nm were also measured and plotted against time, 3, 5, and 7 days, for treatment of PAM-Ag1, PAM-BN3, and PAM-Ag-BN in chondrocyte C28/I2 cells.

2.1.7.2. Antibacterial activity using E. coli. The antibacterial activity of PAM-Ag1, PAM-BN3 and PAM-Ag-BN was tested using *E. coli* Gram-negative bacteria. The samples were first washed with 70% alcohol and then in MilliQ water. The hydrogel samples were seeded in *E. coli* bacterial culture (100 μL, 1.0×10^6 CFU ml^{-1}) in a 24-well culture plate and incubated at 37 °C for 3 days. After the incubation, the samples were washed to remove adherent bacteria. The quantitative estimation of the cultured samples was done by an MTT assay. The MTT reagent was added to the cultured samples and incubated for 3 h at 37 °C followed by dissolution using DMSO, and the absorbance was measured at 570 nm wavelength using a microplate reader.

2.2. Computation methodology

The DFT level of approach plays a significant role in understanding and characterizing all-encompassing atomistic properties, especially the interfacial interactions between two components in the dimer composite (PAM-Ag and PAM-BNOH) and trimer composite (PAM-Ag-BNOH hybrid hydrogel) models have been studied thoroughly in this research work. An organized quantum chemical calculation (QCC) has been done to reconnoitring some noteworthy and fascinating features such as structural stability [*via* interaction energy, MNIs, and noncovalent interactions (NCIs) including vdW interactions] and electronic properties. The electronic structure calculations were commenced by considering three parent moieties chosen as monomer models (PAM, Ag, and BNOH) in the present work. Afterwards, the theoretical building of two dimer composite models (PAM-Ag and PAM-BNOH) took place and then finally computational designing and quantum computation of a trimer composite model (PAM-Ag-BNOH) was performed where the existence of bonding and nonbonding interfacial interactions was probed. Optimization and frequency (positive for all vibrations modes) calculations of all three monomer constituents (PAM, Ag, and BNOH), dimer (PAM-Ag and PAM-BNOH) and trimer (PAM-Ag-BNOH) composite models were done using an electronic structure calculation package (Gaussian 09) in the framework of the DFT level of approach.[37] Due to the reasonably large size of the dimer and trimer composite models and high computational cost, the quantum mechanical calculations have been executed with the employment of the DFT approach using the B3LYP/6-31G method.[38,39] To acquire profound insights into the kind and nature of the interfacial interactions between two components as well as intramolecular interactions taking part in the same molecular entity, the NCI-plot tool was applied.[40,41]

3. Results and discussion

3.1. Experimental analysis

3.1.1. Surface morphology, phase and functional group analysis of dimer hydrogels. The cross sections of the dimer hydrogels (PAM-Ag1, PAM-Ag3, PAM-Ag5, PAM-BN1, PAM-BN3, and PAM-BN5) were used for the observation of surface morphology (Fig. 2A). The Ag-based composite hydrogels show the dispersion of Ag nanoparticles in the PAM matrix. The PAM-Ag1 (Fig. 2A, a) hydrogel exhibits less amounts of Ag nanoparticles (0.1 wt% of Ag). At the same time, the highest content of Ag can be seen in PAM-Ag5 (0.5 wt% of Ag), which signifies some agglomerated features of Ag in PAM (Fig. 2A, c). Fig. 2A, d, e shows the distribution of BNOH particles in the PAM matrix. Large aggregates of smaller, flaky particles with irregularly formed edges, measuring around 120 nm in thickness, make up BNOH particles. The functionalized hBN particles display a clear layered structure with improved stacking dispersion performance. The amount of BNOH is significantly higher in PAM-BN5 (0.5 wt% of BNOH, Fig. 2A, f) than in PAM-BN1 (Fig. 2A, d) and PAM-BN3 (Fig. 2A, e). The confirmation of the presence of Ag nanoparticles and BNOH in a PAM matrix can be confirmed by elemental mapping and energy-dispersive X-ray spectroscopy (EDS) or XRD spectrum. The uniform distribution of Ag along with other existing elements such as C, O, and N (due to PAM hydrogel) in PAM-Ag1 can be observed from elemental mapping (Fig. 2B, b–e) and EDS plot (Fig. 2B, f). The PAM-BN3 sample further confirmed the existence of B, N, C and O elements (Fig. 2C, b–e) and EDS (Fig. 2C, f) in the PAM matrix. A similar pattern of Ag nanoparticles and BNOH particles in a hydrogel matrix was observed by other researchers in their work.[42,43]

The XRD was used to confirm the retention of phases in the synthesis of PAM-based hydrogel composites (Fig. 3). The broad humps in the samples were due to the presence of an amorphous polymeric material, polyacrylamide.[44] Furthermore, featured peaks of Ag are presented in PAM-Ag1, PAM-Ag3 and PAM-Ag5 dimer hydrogels as (210), (110), (122), (111), (200), (220) and (311) crystallographic planes at ~27.7°, ~32.1°, ~34.2°, ~38.4°, 44.5°, 67.7° and 77.4°, respectively.[45–47] Amorphous bulk polyacrylamide reduced the intensity of metallic or ceramic peaks.[48] The phases of BNOH and PAM-BN-based hydrogels were further confirmed and it was demonstrated that the specific peak (002 crystalline phase) of BN is present at 26.7°.[49,50]

After determining the surface morphology and phases in all Ag and BNOH-based PAM hydrogels, FT-IR spectra were used to identify the functional group and bonding present in the dimer hydrogels (Fig. 4). Fig. 4 represents the spectrum of PAM-Ag1, PAM-Ag3, and PAM-Ag5, and it is clear that the strong vibration bond at ~3353 cm^{-1} is due to the O–H bond, while the characteristic N–H stretching vibration is observed at ~2936 cm^{-1} due to the presence of amide group in the PAM hydrogel. The absorption at ~1662 cm^{-1} embodies the C═O stretching in the $-CONH_2$ group and the shoulder peak at ~1560 cm^{-1} is due to NH_2 bending. These peaks also confirmed the stability of PAM under reactive conditions. The bonding between Ag and oxygen is present as Ag–O at 840 cm^{-1}.[51,52] This bonding is considered as relatively weak bonding due to the minimum overlap between metal and non-metal. The presence of a bigger d orbital in Ag is responsible for the least overlapping. The shoulder peaks in all the composites at ~3184 cm^{-1} illustrate the complexation between the reinforcements and PAM matrix.[53–55] Next to the PAM-Ag dimer composites, PAM-BN composites also display characteristic bands (Fig. 4). The peaks for PAM are similar to that of PAM-Ag hydrogels. The BNOH powder contains peaks at ~3402 cm^{-1} due to B–OH stretching, ~1371 cm^{-1} due to B–O in-plane bending and at ~786 cm^{-1} due to B–O···H out-of-plane bending. In PAM-BN composites, an intense peak at ~3390 cm^{-1} represents O–H stretching peak. The O–H peak is more intense due to the higher polarity of the OH group than the NH group. The B–O in-plane peak and B–O···H out-of-plane bending are shifted from ~1371 cm^{-1} (BNOH) to ~1375–1406 cm^{-1} (PAM-BN1, PAM-BN3 and PAM-BN5) and from ~786 cm^{-1} (PAM) to ~795 cm^{-1} in composites.[49,56,57] The shifting is due to the formation of hydrogel bonding between

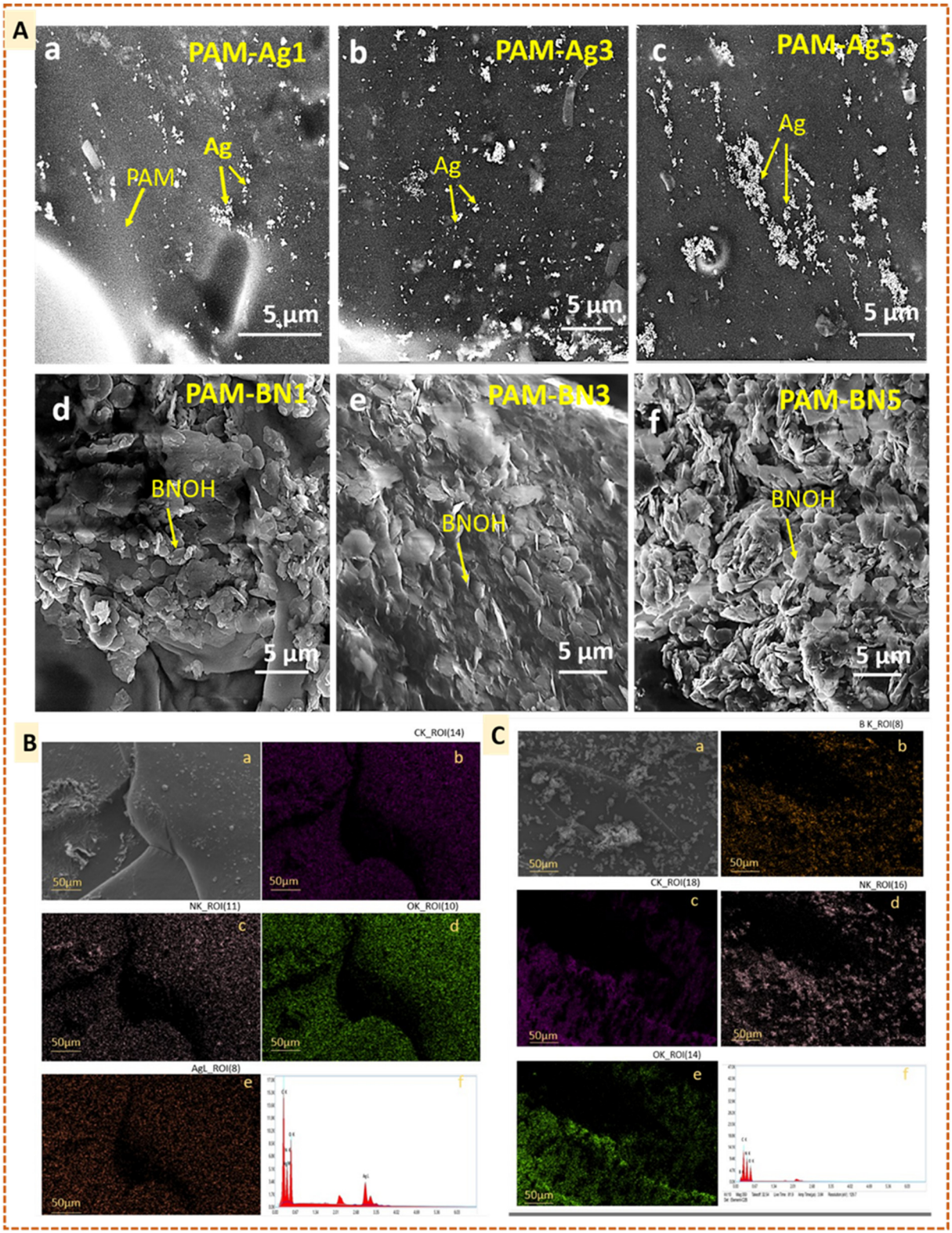

Fig. 2 (A) SEM images of (a) PAM-Ag1, (b) PAM-Ag3, (c) PAM-Ag5, (d) PAM-BN1, (e) PAM-BN3, and (f) PAM-BN5. (B) Elemental mapping of the PAM-Ag1 composite showing (a) surface morphology, (b) elemental C distribution, (c) elemental N distribution, (d) elemental O distribution, (e) elemental Ag distribution, and (f) EDS. (C) Elemental mapping of the PAM-BN3 composite showing (a) surface morphology, (b) elemental B distribution, (c) elemental C distribution, (d) elemental N distribution, (e) elemental O distribution, and (f) EDS.

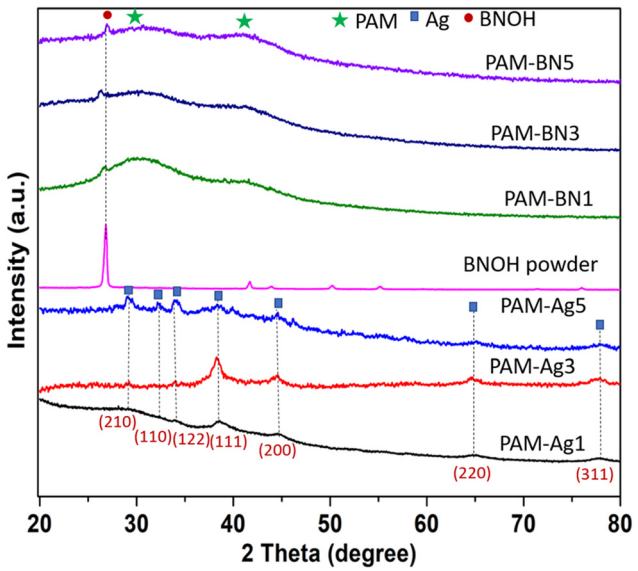

Fig. 3 XRD pattern for PAM-Ag1, PAM-Ag3, PAM-Ag5, BNOH powder, PAM-BN1, PAM-BN3 and PAM-BN5 dimer hydrogel composites.

BNOH and PAM hydrogel.[58] Thus, it is clear that a greater number of OH bonding is formed in PAM-BN-based hydrogel composites than that of PAM-Ag-based hydrogels. A comprehensive study based on the computational experiments for the interfacial (bonding and nonbonding) interactions are facilitated in the computational section.

3.1.2. Hydrophilicity, surface roughness, swelling and degradation performance of dimer hydrogels. The hydrophilicity of the biomaterials is an essential performance as it is liable for the proliferation of cellular responses and protein adsorption in the biological atmosphere, which results in enhanced bone formation by the implants.[59,60] The contact angle (CA) values express the hydrophilicity/hydrophobicity of any material. The hydrophilicity or hydrophobicity depends on the surface roughness of the materials. When using AFM, topographical bright and edged areas may be easily distinguished from the sublayer, providing additional evidence of surface irregularity (Fig. 5A). In the case of Ag-based PAM composites, the highest hydrophilic behaviour was shown by PAM-Ag1 (29°) when compared to PAM-Ag3 (45°) and PAM-Ag5 (62°). The Ag nanoparticles are hydrophobic in nature[61] and PAM is hydrophilic, so the lower content of Ag in PAM makes PAM-Ag1 more hydrophilic than other Ag-based hydrogels. Furthermore, the hBN is also considered as hydrophobic, but functionalization of hBN with OH group converts hydrophobic nature to hydrophilic.[62] Therefore, a higher content of BN (0.5 wt%) in PAM-BN5 resulted in the highest hydrophilicity, having the lowest CA (22°) when compared to other PAM-BN compositions (Fig. 5B). The CA of PAM-BN5 is lower even than that of PAM-Ag1 due to the hydrophilic nature of BNOH and PAM while the hydrophobic nature of Ag shows higher CA. Similar values of CA of Ag and BNOH-based composites are also reported by Sharmin *et al.*[63] and Gao *et al.*[64] in their previous works. In general, the anti-wetting behaviour of designed surfaces was enhanced by increasing the surface roughness value (Fig. 5C). The lower roughness in the case of PAM-Ag1 and PAM-BN5 resulted in reduced contact angle and thus higher hydrophilicity of the materials. A similar relationship between roughness and contact angle values for hydrogel samples was also reported by Luca *et al.*,[65] which showed that the enhanced surface roughness of the hydrogel samples offered increased hydrophobicity.

The swelling behaviour of hydrogels is measured by immersing the samples in PBS and weighing them after different time intervals. The compact network of the hydrogel, surface area, particle size, *etc.*, can alter the swelling rate of the materials.[66] The swelling behaviour of the hydrogel samples was observed to be rapid during the initial hours of immersion. This rapid swelling is presented by the dotted circle in Fig. 6a and the enlarged view of the dotted portion is presented in Fig. 6b. The swelling ratio was increased almost two-fold from 0.5 h to 1.0 h to 1.5 h for all the samples (Fig. 6b).

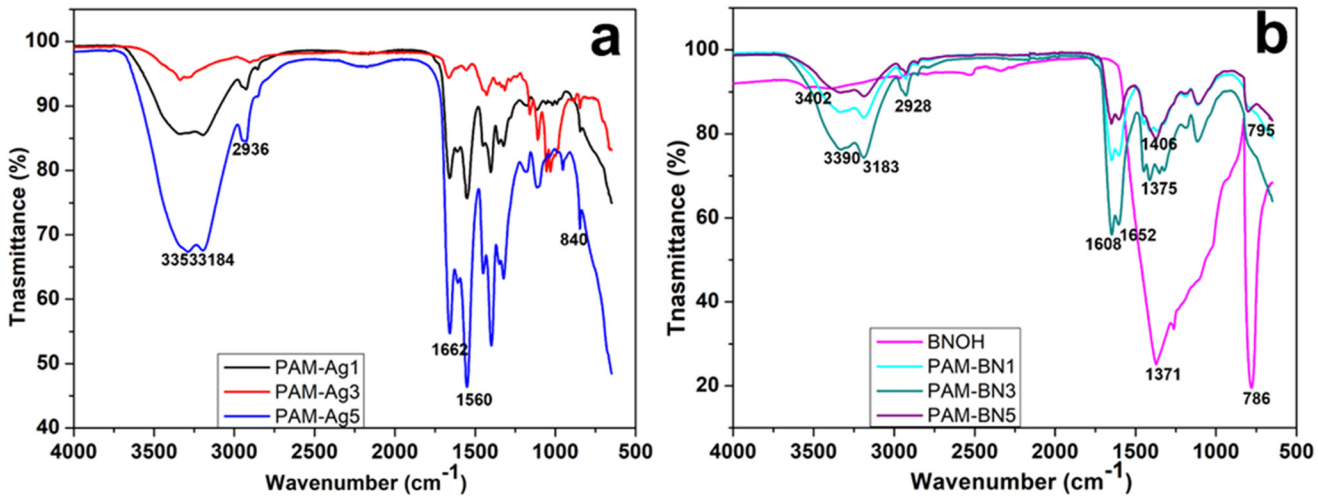

Fig. 4 FT-IR spectra for (a) PAM-Ag1, PAM-Ag3, PAM-Ag5, (b) BNOH powder, PAM-BN1, PAM-BN3 and PAM-BN5 dimer hydrogels.

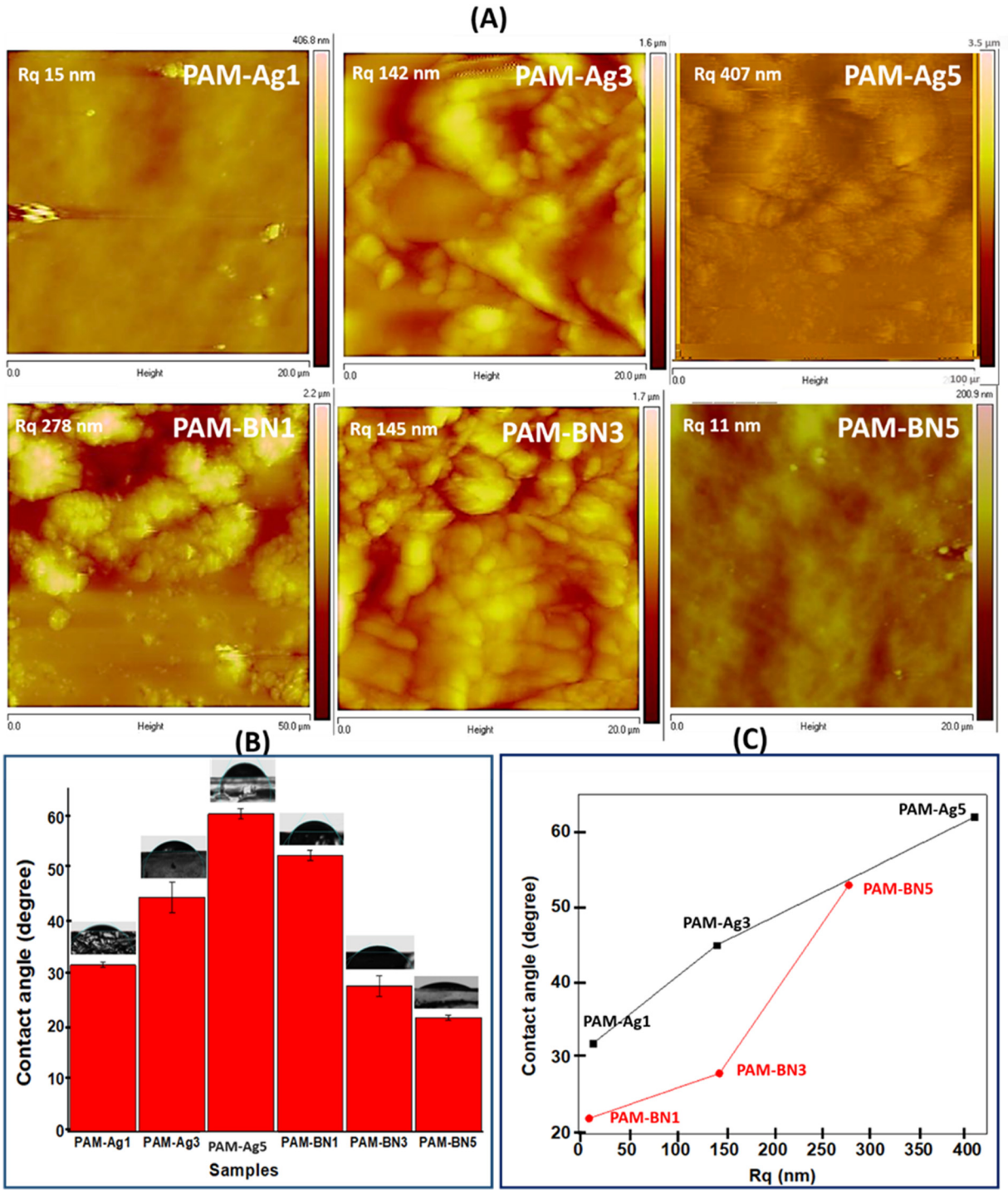

Fig. 5 (A) AFM topographies of the engineered hydrogel surfaces, (B) contact angle values and (C) connections between surface roughness and water contact angles measured through all designed Ag and BN-based hydrogel samples.

The equilibrium swelling was obtained for all the composites after 10 h of immersion in PBS (Fig. 6a). The PAM-Ag and PAM-BN-based composites with non-swelling behaviour (after equilibrium) are referred to as stable biomaterials and showed a momentous feature for cartilage repair applications. The higher content of Ag and BNOH in PAM-Ag5 and PAM-BN5, respectively exhibited less extent of swelling (Fig. 6a) due to the higher number of covalent crosslinking between PAM and Ag as well as with BNOH, which makes a compact structure of PAM-Ag5 and PAM-BN5 and limits the swelling in PBS. However, the lowest swelling ratio in PAM-BN5 was due to the higher number of bonds formed between BNOH and PAM than that of PAM and Ag (described in FTIR spectroscopy).

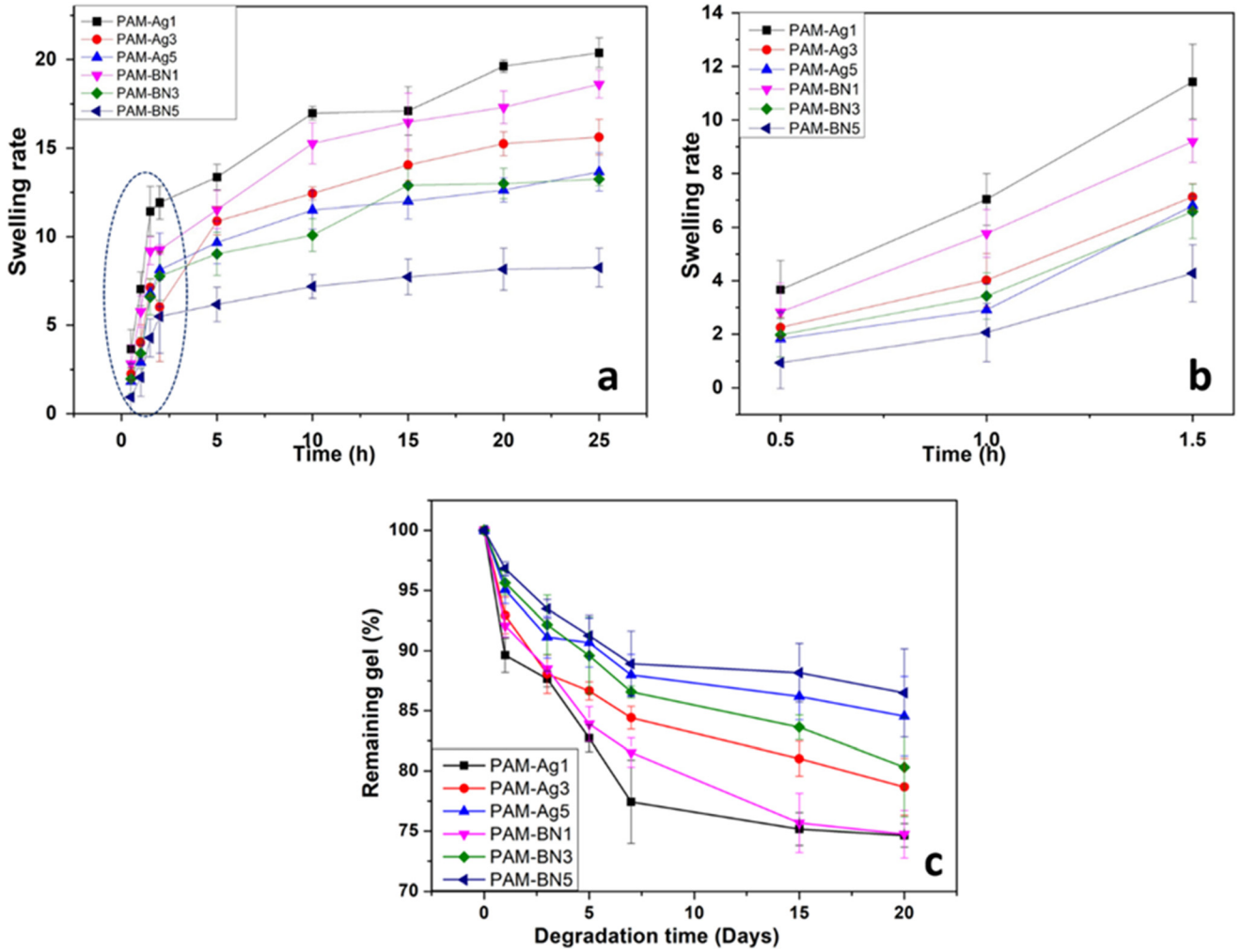

Fig. 6 (a) Swelling ratio, (b) enlarged version (dotted circle of plot a) of the swelling ratio data during initial hours of immersion of the hydrogels and (c) degradation behaviour of PAM-Ag1, PAM-Ag3, PAM-Ag5, BNOH powder, PAM-BN1, PAM-BN3 and PAM-BN5 dimer hydrogels.

Degradation (*in vitro*) of the hydrogel samples was determined in terms of % of the remaining gel after 0, 5, 10, 15 and 20 days in PBS. Fig. 6b recommends that there is huge weight loss in the hydrogels in the first week of immersion while the weight is constant for the gels after 10 days in PBS. The prepared dimer hydrogels exhibited an ideal % of remaining gel (~75%) for cartilage applications after 20 days of immersion in PBS. The higher content of Ag and BN (PAM-Ag5 and PAM-BN5) showed reduced damage in materials having the highest percentage of remaining gels of ~90 due to the rigid structure of the samples (Fig. 6b). The lower % of remaining gel in PAM-Ag1 caused enhanced hydrolysis due to the highest absorption of water during the swelling process.

3.1.3. Compression experiment analysis. The strong mechanical strength is a very crucial phenomenon for any bone implant. The comparison of strength between the hydrogel samples was done using a compression test and it was found that PAM-Ag1 showed a higher compressive strength (~0.21 MPa) in Ag-based PAM hydrogel composites. The concentration of Ag in PAM-Ag1 was the lowest and the distribution of Ag nanoparticles within the PAM matrix is adequate, which offers a significant interfacial bonding between Ag and PAM with an Ag–O bond. The compressive strength started decreasing (0.19 MPa for 0.3 wt% and 0.15 MPa for 0.5 wt%) when the concentration of Ag was increased from 0.1 wt% to 0.5 wt% (Table 1). The enhanced concentration of Ag nanoparticles in PAM resulted in agglomeration, and thus, impacted reduced strength. Moreover, the addition of BNOH

Table 1 Compressive strength and Young's modulus of the dimer hydrogels

Samples	The concentration of Ag and BNOH (wt%)	Compressive strength (MPa)	*E* (MPa)
PAM-Ag1	0.1	0.22 ± 0.01	0.19 ± 0.01
PAM-Ag3	0.3	0.20 ± 0.02	0.21 ± 0.01
PAM-Ag5	0.5	0.16 ± 0.01	0.14 ± 0.00
PAM-BN1	0.1	0.21 ± 0.01	0.20 ± 0.01
PAM-BN3	0.3	0.26 ± 0.01	0.27 ± 0.00
PAM-BN5	0.5	0.17 ± 0.00	0.15 ± 0.01

Table 2 Potentiodynamic parameters of PAM, PAM-Ag1, PAM-BN3 and PAM-Ag-BN hydrogels

Samples	$i_{corr} \times 10^{-5}$ (A cm^{-2})	E_{corr} (V)	β_a (V per decade)	β_c (V per decade)	R_{PD} (Ω cm^2)
PAM	7.45 ± 0.20	−1.08 ± 0.00	5.39 ± 1.12	10.83 ± 0.91	20 975
PAM-Ag1	5.85 ± 0.21	−1.03 ± 0.02	6.48 ± 0.98	8.10 ± 2.76	26 721
PAM-BN3	4.21 ± 0.69	−1.07 ± 0.00	17.54 ± 2.02	6.096 ± 2.19	46 623
PAM-Ag-BN	2.65 ± 0.21	−1.04 ± 0.00	22.86 ± 1.10	3.94 ± 1.98	55 067

in PAM contributed better mechanical strength than PAM-Ag1. The micron-sized BNOH particles exhibited the highest strength of 0.25 MPa with 0.3 wt% of BNOH in PAM (PAM-BN3, Table 2) due to the good dispersion of BNOH in PAM. The PAM-BN1 with a lower concentration (0.1 wt%) cannot contribute towards the strength sufficiently, while the excess concentration of BNOH (0.5 wt%) leads to pulling out of BNOH micron particles from the PAM matrix during compression.[50] The enhanced mechanical performance of BNOH over Ag was due to the strong interfacial interaction of BN with PAM. BN was functionalized and BNOH furnished several hydrogen bonds with the PAM matrix (discussed in section 3.1.1). The strong B–O···H bonding between BNOH and PAM resulted in a higher compressive strength (a detailed discussion is given in the computational analysis section). Young's modulus (E) of the hydrogel composites was calculated from the obtained stress–strain curve to further confirm the strength of the hydrogels. Young's modulus was also observed higher for the PAM-BN3 composite (0.27 MPa) than other hydrogel composites (Table 1). Thus, based on the mechanical strength of the hydrogels, a trimer composite was fabricated using a dried mass of PAM and immersing it in 0.1 wt% of Ag and 0.3 wt% of BNOH solution. Further testing was done on three samples, namely PAM-Ag1, PAM-BN3 and PAM-Ag-BN.

3.1.4. Morphology, phase and compression test of trimer composites. The trimer composite (PAM-Ag-BN) was characterized and the surface morphology and phase were observed using SEM, XRD and elemental mapping. The refined distribution of Ag and BNOH was observed from the surface morphology of hydrogel (Fig. S2Ai†). The XRD (Fig. S2Aii†) of PAM-Ag-BN showed the specific peaks of PAM, Ag and BN, (as already discussed in section 3.1.1), showing the phase retention of nanoparticles in PAM after the synthesis. The uniform distribution of Ag and BN in the PAM matrix was further confirmed from Fig. S2Aiii.† Furthermore, the compressive strength and Young's modulus of PAM-Ag-BN were tested and compared with the dimer hydrogels. PAM-Ag-BN exhibited better maximum strength (0.31 MPa) and Young's modulus (0.29 MPa) than those of dimer composites (maximum strength was 0.26 MPa for PAM-BN3, Table 1). The higher strength attained by the trimer hydrogel composite was due to the synergistic effect of nano- and micron-sized nanoparticles in PAM. The instantaneous interactions of Ag and BNOH with PAM established B–O···H and Ag–O specific bonds and produced strong interfacial interaction.

The compressive strength exhibited by the PAM-Ag-BN trimer composite is better than that of the Ag and BN-based hydrogel composites reported earlier in the literature. For example, Gao *et al.*[64] prepared boron nitride nanofibers (BNNF) with poly(vinyl alcohol) by a one-pot assembly method. The BNNF was functionalized with a hydroxyl group. The concentration of BNNF varied from 1.25 wt% to 2.75 wt%. In addition, it was observed that with the increase in the concentration of BNNF, the compressive strength of the hydrogel composites was enhanced. The maximum strength attained by the hydrogel was 0.14 MPa (0.31 MPa for trimer composite in the present work and 0.26 MPa for dimer composites of PAM-BN3). The different shapes of Ag nanoparticles were doped with the PAM hydrogel and the mechanical strength of the composite hydrogel was tested by Ferrag *et al.*[67] The shapes of Ag nanoparticles were synthesized by one-pot synthesis and Young's modulus was observed for all types of PAM-Ag composites. The highest modulus was obtained as 70 kPa (0.07 MPa) for the sphere shape of Ag nanoparticles in the PAM matrix. The values obtained in the present work (0.29 MPa for trimer and 0.27 MPa for dimer, Table 1) are much improved from the reported literature. Moreover, the work reported by Butylina *et al.*[68] showed that polyvinyl alcohol was grafted with nanocrystalline cellulose and the stress–strain curve was used to calculate the elastic modulus values. In this work also, the maximum obtained value for elastic modulus was 0.23 MPa (0.29 MPa for trimer; see Table 1 for comparison).

3.1.5. Electrochemical analysis of the hydrogel samples. The implants mostly based on polymers can start dissolving in body fluids after a certain time period. Besides, cells and tissues, human body fluid contains various inorganic constituents such as phosphates, sugar, and proteins, which may cause degradation or corrosion to any polymeric or metal alloy implants.[35] Therefore, it is essential to evaluate the effect of these components on implant material by using electrochemical studies in simulated body fluid (SBF), which possesses a similar ionic composition to human plasma. The titanium alloy coated with four hydrogels (PAM, PAM-Ag1, PAM-BN3 and PAM-Ag-BN) was stabilized with constant potential values using open circuit potential followed by the execution of potentiodynamic polarization studies and the observation of surface morphology of samples after corrosion.

The potentiodynamic polarization was performed on the samples and the Tafel polarization curve is presented in Fig. 7. The extrapolation of the Tafel polarization curve was done to obtain electrochemical parameters such as corrosion potential (E_{corr}), corrosion current density (i_{corr}), and anodic and cathodic Tafel slopes β_a and β_c, respectively. The Stern–Geary

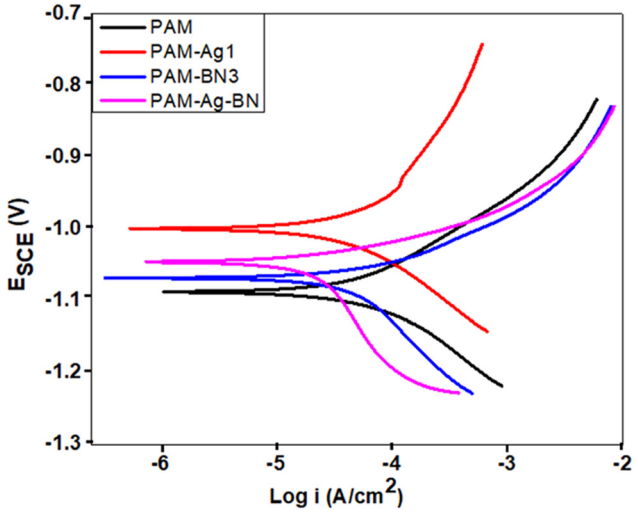

Fig. 7 Potentiodynamic polarization curve of PAM, PAM-Ag1, PAM-BN3 and PAM-Ag-BN hydrogels.

equation was used to calculate the polarization resistance (R_{PD}).[69]

$$R_{PD} = \frac{\beta_a \beta_c}{2.303 i_{corr}(\beta_a + \beta_c)} \quad (4)$$

The corrosion current density (i_{corr}) was observed minimum (2.65 A cm^{-2}) for trimer composite (PAM-Ag-BN). The higher i_{corr} was obtained for bare PAM (Table 2). The corrosion potential was slightly shifted toward positive values for composite hydrogels when compared to bare PAM (Table 2). The polarization resistance was calculated to be highest for PAM-Ag-BN (55067 Ω cm^2) than other hydrogel composites. Among dimer composites, PAM-BN3 showed improved corrosion resistance than PAM-Ag1. The enhanced corrosion resistance of BN over Ag was due to the strong interlocking of BN particles with the PAM matrix *via* hydrogen bonding, while the synergistic effect of Ag nanoparticles and BN micro-particles with combined bonding of Ag and BNOH with PAM established maximum corrosive resistance behaviour of the trimer composite.

The potentiodynamic studies destroyed the sample surface. The extent of damage after corrosion testing was demonstrated by the observation of the surface morphology of the hydrogel samples. The top surface of PAM and PAM-Ag1 showed the macro pits and cracks (Fig. 8a and b) when compared to PAM-BN3 (Fig. 8c) due to the poor mechanical strength and bonding of Ag, which behaves as an active site for the pitting corrosion and deteriorate the surface. The extent of mutilation was the least for the PAM-Ag-BN trimer composite (Fig. 8d) due to the synergistic effect of small (μm and nm-sized) reinforcements, which contributed strong mechanical interlocking with PAM. These additives restricted the defect corrosion by filling the holes and crevices of PAM resulting in an amended surface property of composite hydrogel. Second, these particles inhibited the localized corrosion and propagation of defects across the surface of the hydrogel.

3.1.6. Biomineralization and self-healing of the hydrogel composites *in vitro*. The ability of cartilage implants to form calcium-phosphate crystals or apatite is an essential performance to confirm the bioactivity of the implant material. The cartilage tissue is supported by apatite, which also promotes bone integration and the formation of osteogenic tissue.[70] The formation of apatite on the surface of the hydrogels can be observed in Fig. 9. The formation of apatite crystals was higher in trimer composite hydrogels due to its advanced biocompatibility (having both bioactive Ag and BNOH particles).

The XRD pattern of hydrogels (Fig. 10) further confirmed the development of apatite on the hydrogel's surface. The specified peaks of apatite were present with crystalline phases of (211), (202), (200), (222) and (213) at 2θ of 31.2°, 34.5°, 42.2°, 48.9° and 50.5°, respectively. Therefore, the higher content of apatite in trimer composite hydrogels (PAM-Ag-BN) showed signs of osteoconduction through noteworthy bone formation ability in SBF and can be ideal bioactive cartilage regeneration material once implanted *in vivo*.

The self-healing of the hydrogel was confirmed by cutting the trimer sample (images are provided in ESI S2B†). The addition of water drops on the cracked sample provides hydration, and according to the Gibbs–Donnan effect, the swelling and expanding of the polymer network occur by osmosis. The capillary action makes the pores shrink and gives a compact structure to the hydrogel. The healed sample was stretched by hands and showed significant curing of the cracked surface of the hydrogel sample. The compression test was performed on the healed sample and 0.11 MPa of compressive strength was exhibited by the sample. Thus, the hydrogel sample with amended self-healing properties can be a potential cartilage implant with the capability to accelerate the natural curing in the contiguous tissue.

3.1.7. Cytotoxicity assay

3.1.7.1. Cytotoxicity assessment on chondrocyte cells. The influence of PAM-Ag1, PAM-BN3 and PAM-Ag-BN on the cytotoxicity of chondrocyte C28/I2 cells is shown in Fig. 11. PAM-Ag1 showed 95.8%, 95.5% and 94.5%, while PAM-BN3 exhibited 97.4%, 97.1% and 96.4% cell viability for 3, 5 and 7 days, respectively. The higher call viability in PAM-BN3 was due to the functionalization of hexagonal boron nitride with the OH group. PAM-Ag-BN displayed 98.5%, 98% and 97.3% cell viability for 3, 5 and 7 days, respectively. The synergistic effect of Ag and functionalized BN resulted in a higher % of cell viability for the PAM-Ag-BN trimer composite. Using biocompatible component-conjugated nanoparticles is emerging as an attractive strategy for higher cell viability as well as combating various pathogens. PAM-Ag1, PAM-BN3 and PAM-Ag-BN display a minor difference in cell viability and inhibition capacity, showing biocompatibility and non-toxicity for all the samples. The minor increment in the cell viability of PAM-Ag-BN was due to the synergistic effect of Ag and functionalized BN because Ag nanoparticles are well-known biomaterials and hydroxylated BN can enhance the water solubility of BN and thus the bioactivity. Several studies have effectively employed a mixture of two or more therapy components as their

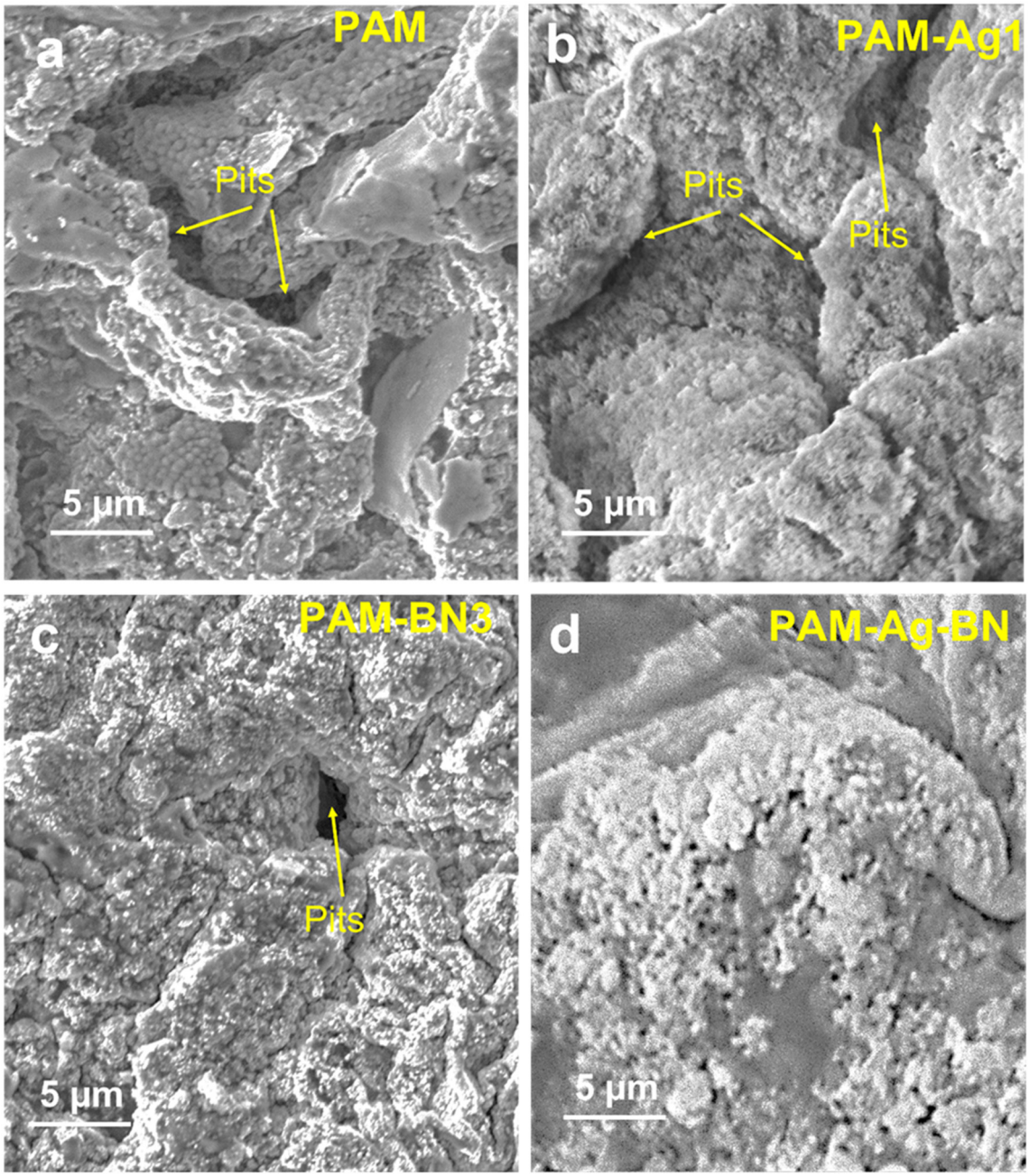

Fig. 8 Scanning electron microscopic images of the top surface of (a) PAM, (b) PAM-Ag1, (c) PAM-BN3 and (d) PAM-Ag-BN hydrogels after corrosion testing.

method[71,72] for the improvement of biocompatibility. This strategy seeks to either create a synergistic impact or extend the cell viability and antibacterial activity. Gudz *et al.*[73] also reported the synergistic effect of the combination of Ag and BN together for biomedical applications. Moreover, MTT values show non-significant differences between PAM-Ag1, PAM-BN3 and PAM-Ag-BN over time of incubation (Fig. 11d). The OD values at 570 nm were increasing, proving chondrocyte C28/I2 cell growth in all hydrogel samples over 3, 5, and 7 days. The treatment of hydrogel composites showed non-toxic and non-significant differences between groups. Fig. 12 displays the microscopic images of PAM-Ag1, PAM-BN3 and PAM-Ag-BN treatment on chondrocyte C28/I2 cells for 3 days. These images confirm that cell proliferation is not affected by treatment with good biocompatibility.

3.1.7.2. Antimicrobial analysis of hydrogels. The antimicrobial activity of PAM-Ag1, PAM-BN3 and PAM-Ag-BN against *E. coli* bacteria was measured quantitatively by the MTT assay. The MTT assay results indicated that the inhibition of bacterial growth was more than 80% for all the samples (Fig. 13). The PAM-Ag-BN showed the highest *E. coli* bacterial inhibition of 85%, while PAM-BN3 and PAM-Ag1 showed

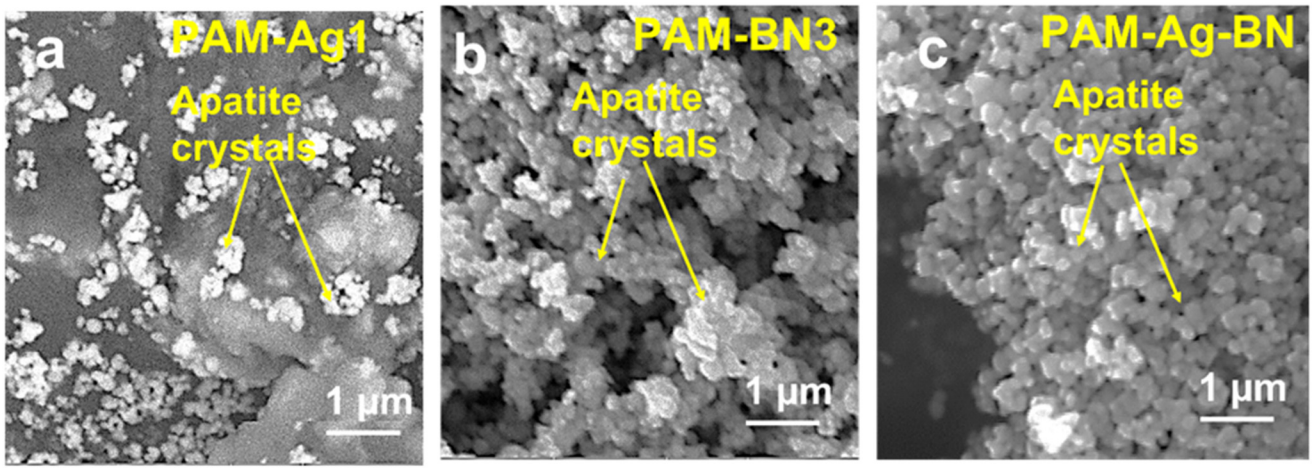

Fig. 9 Surface morphology of (a) PAM-Ag1, (b) PAM-BN3 and (c) PAM-Ag-BN hydrogels showing apatite formation.

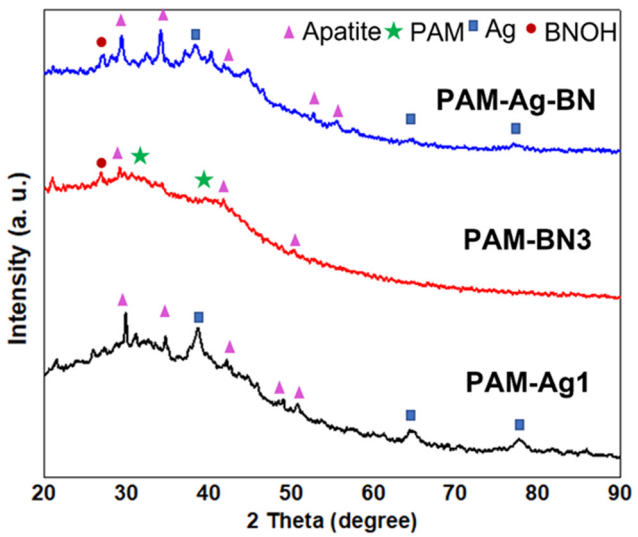

Fig. 10 XRD pattern of the PAM-Ag1, PAM-BN3 and PAM-Ag-BN hydrogel samples showing specific apatite peaks.

83.3% and 81.8%, bacterial inhibition respectively. These results indicate that PAM-Ag1, PAM-BN3 and PAM-Ag-BN have good antibacterial activity and can be used in tissue engineering related to cartilage repair.

3.2. Computational analysis

To gain profound insights into structural properties, bonding (metal–metal and metal-nonmetal) and nonbonding interaction(s) [like H-bonds (HBs) and vdW], and electronic features of all five moieties (two components and three composite models), three techniques [two based on the NCI-plot (3D-isosurface map and 2D-scatter plot) and one based on the QTAIM tool] were used and various interesting intramolecular H-bonding and vdW interactions were observed which self-stabilize the parent entities (particularly, the PAM and BNOH). Details about the NCI-plot (3D isosurface map and 2D scatter plot) can be viewed in sections 1 and 2 of the ESI,† respectively (see references in the ESI†). Regarding the NCI-plots, here it is important to mention that the dark blue colour as displayed in both the 3D-isosurface map and 2D-scatter plot shows interactions (either moderate metal–metal or metal-nonmetal or very strong H-bonding interaction), whereas the light blue (or bluish-green) colour indicates the moderate (or weak) H-bonding interactions. Moreover, the green colour gives the impression of the extremely weak H-bonding and vdW type of interaction. The occurrence of steric effect is clearly exposed by the low-gradient spikes appearing at the positive side (0 to 0.03 au). Such effect as expressed by the red ellipsoid describes the electron density depletion, which is due to the electrostatic repulsion.

Moreover, some selected and important QTAIM topological parameters having the capability to distinguish the kind, nature, and strength of interactions have been discussed. The sign of the Laplacian of the electron density at a bond critical point (BCP), $\nabla^2(\rho)$, exposes whether the charge is concentrated as in 'shared' manner (referred as a covalent) interaction, *i.e.* $\nabla^2(\rho) < 0$ and $\rho > 0.1$ atomic unit (au).[74] In the case of a depleted or 'closed shell' (H-bonding, ionic, and vdW) interaction, $\nabla^2(\rho) > 0$, whereas the ρ value is generally small (~order of 10^{-2} au for H-bonding and 10^{-3} au for a vdW interaction). In the QTAIM molecular graph, the big sphere (in light blue colour) shows the bond path (BP) as a stabilization interaction in all six probed cases (component to dimers to trimers). It should be noted that in the case of dimer and trimer composite models, the big sphere in blue colour (illustrating the BCPs) is shown for the interfacial interactions only. It is worth to mention that the bond path length (BPL) is always equal to or greater than the bond length (BL) between two atomic interactions.

3.2.1. Constituents as component models

3.2.1.1. Structural and electronic feature analyses. At first, to get the equilibrium structures of the parent species (*i.e.* component models: PAM, Ag, and BNOH), frequency calculations were executed followed by the optimization procedure. The optimized structures and parameters of the PAM, Ag, and

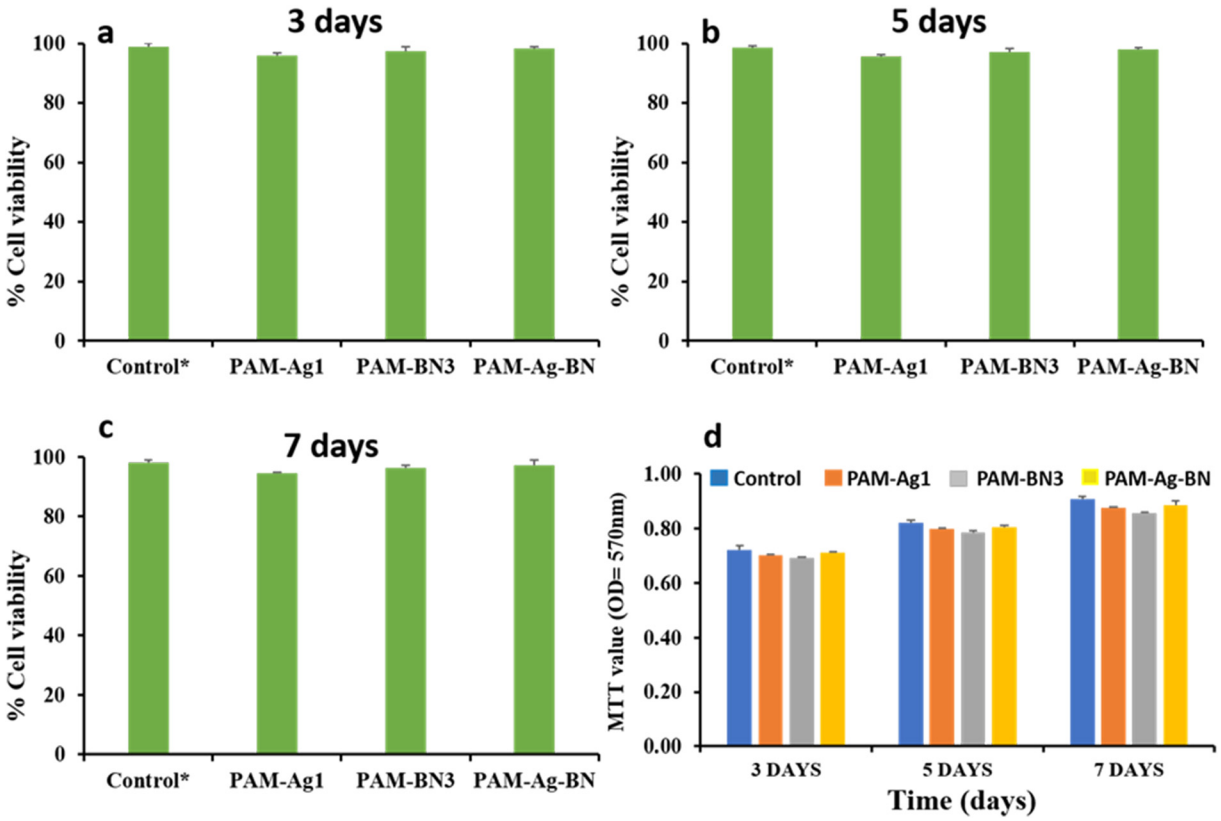

Fig. 11 Influence of PAM-Ag1, PAM-BN3 and PAM-Ag-BN on chondrocyte C28/I2 cell viability for 3 (a), 5 (b) and 7 (c) days, (d) MTT values overtime of 3, 5 and 7 days with PAM-Ag1, PAM-BN3 and PAM-Ag-BN in chondrocyte C28/I2 cells at OD 570 nm.

BNOH units are shown in Fig. 14 (left) and Table 3 (see the last three row), correspondingly. After getting the equilibrium structure of the Ag assembly (a total of twenty Ag atoms *i.e.* Ag_{20} have been chosen in this research work) and having insights into this component model, a refined QTAIM molecular picture is shown in Fig. S3 of the ESI,† where two front and central Ag atoms and the other Ag atoms of the component model are connected to both front and central Ag atoms and thus constructing one of the parent moieties (here, the Ag_{20} assembly as a monomer unit is referred to as the Ag). The Ag–Ag bond lengths (BLs) range from 2.796 Å to 3.172 Å with respect to two central front Ag atoms. A glimpse of the NCI-plots (3D isosurface map and 2D scatter plot) of the PAM component model is shown in Fig. 14. The 3D-isosurface map (top-middle) of the Ag assembly can be viewed in Fig. 14, where blue colour indicates metal–metal (moderate) interaction between the two Ag atoms, and such findings are further supported by the NCI 2D-scatter plot (top-right) diagram region (ranging from −0.015 au to −0.035 au) as well as the QTAIM molecular graph (see Fig. S3 of the ESI†).

Second, let us have a closer look at the optimized structure of the single unit of the PAM hydrogel model (middle-left). In this component model, there are two types of NCIs [first type is a total of four HBs (two N–H···O and two C–H···O) and the second type is vdW interaction] detected from the NCI-plot tool (3D-isosurface map and 2D-scatter plot), which can be discerned from Fig. 14 and such evidence was further supported using the QTAIM tool (see Fig. S4 of the ESI†). Two types of HBs [one from the NH group (HB distance (HBD): 1.880 Å and BPL: 1.907 Å) and the other from the NH_2 group (HBD: 1.978 Å and BPL: 2.005 Å)] have been detected (see Table 3). The two ∠N–H···O bond angles were analysed as 144.7° and 157.3°. The blue colour discs of the 3D isosurface map (see Fig. 14 at the centre) of the PAM component model illustrate both N–H···O HBs, which is also favoured by the 2D scatter plot (two blue colour spikes ranging between −0.025 au and −0.035 au) for the same (middle-right). Another weak H-bonding interaction such as two C–H···O (HBD: 2.278 Å, 2.317 Å with their respective BPL: 2.299 Å, 2.339 Å) are shown in dark green colour lentil (discs) and spike (lying between −0.01 au to −0.015 au) in the 3D isosurface map and 2D scatter map of the NCI-plot, correspondingly. Moreover, Fig. S4 of the ESI† displays another kind of stabilizing interaction named nonconventional bond path (NBP) (C···O) (BL: 3.129 Å and BPL: 3.141 Å) as shown by the QTAIM approach and also preferred by the NCI-plot tool (*i.e.* kind of vdW interaction shown by the green colour spike in the 2D scatter plot lying between −0.005 au and −0.01 au). Some important and chosen QTAIM topological parameters of the above-mentioned interactions are shown in Table S1 of the ESI.† For example, bond path length (BPL) (2.005 Å) and QTAIM parameters [ρ: 0.026 au, $\nabla^2(\rho)$: +0.084 au, V: −0.022 au, DI: 0.075] of the N–H···O HB show

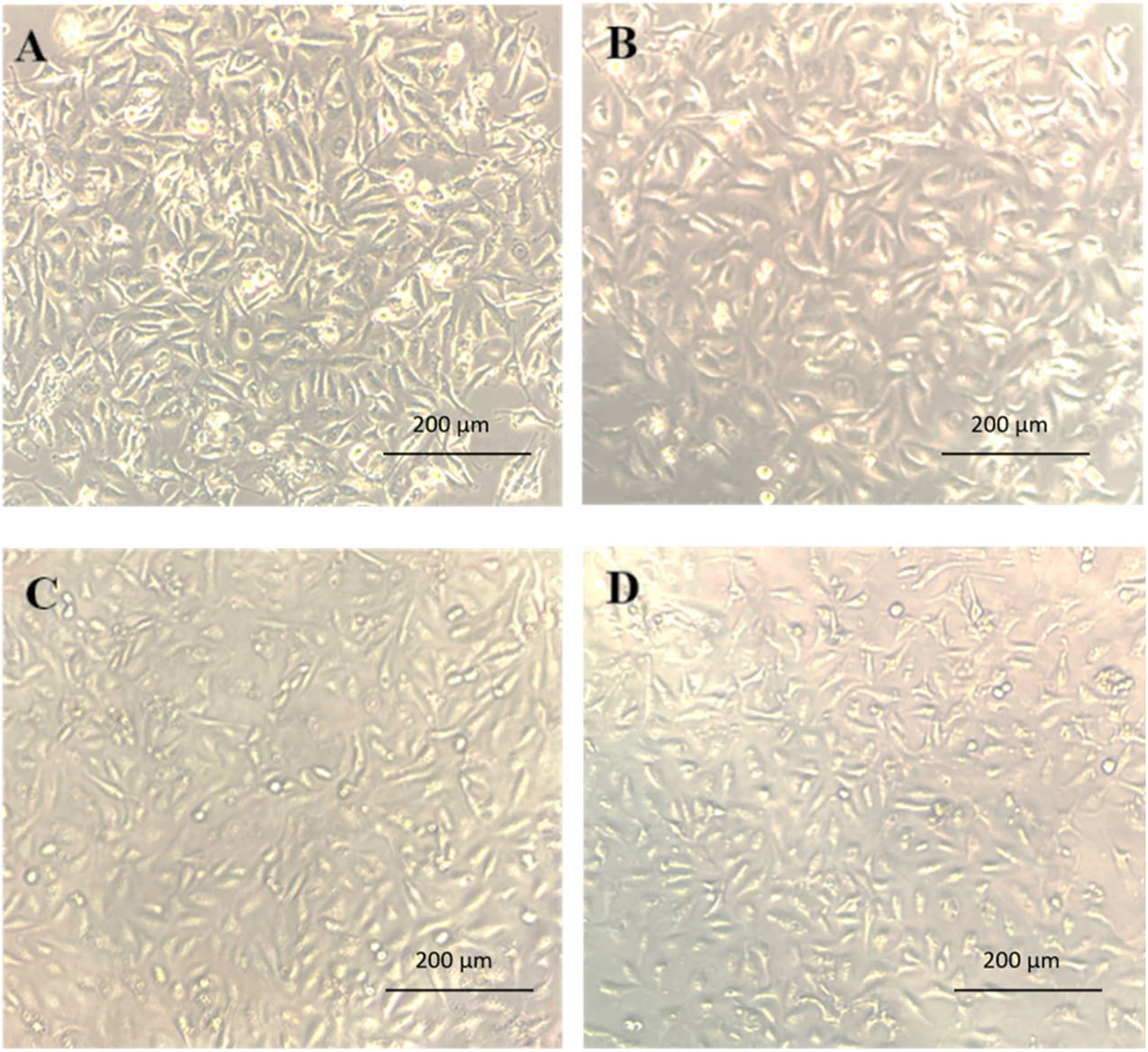

Fig. 12 Microscopic images (40×) of the influence of chondrocyte C28/I2 cell viability on untreated (A), PAM-Ag1 (B), PAM-BN3 (C), and PAM-Ag-BN (D) incubated for 3 days.

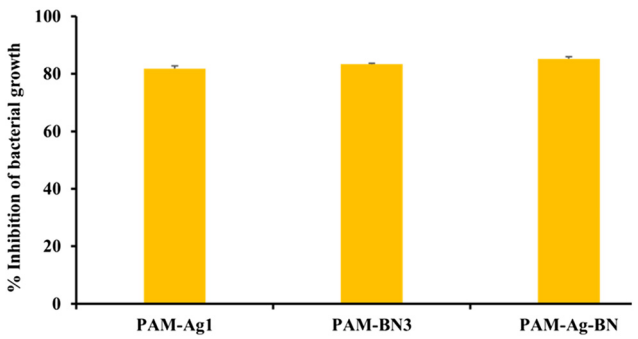

Fig. 13 Percentage inhibition capacity of PAM-Ag1, PAM-BN3, PAM-Ag-BN hydrogel composites for *E. coli* bacteria.

that this NCI is almost two-times stronger than one of the C–H···O HBs (BPL: 2.299 Å, ρ: 0.014 au, $\nabla^2(\rho)$: +0.052 au, V: −0.011 au, DI: 0.048) as expected. The other QTAIM topological parameters such as the Laplacian of electron density, $\nabla^2(\rho)$, local potential energy density, V, (one of the important stabilizing parameters) and bond delocalization index, DI (A, B) are also consistent with the BPL and ρ values.

Third, in the case of the optimized structure of the BNOH moiety (bottom-left of Fig. 14), the B–N bond distances of the outside larger BN (18-membered) ring range from 1.295 Å to 1.398 Å, whereas they lie between 1.6 Å and 1.605 Å for the inside smaller BN (six-membered) ring. A total of six O–H···O H-bonding interactions (three HBs connected to the B atoms

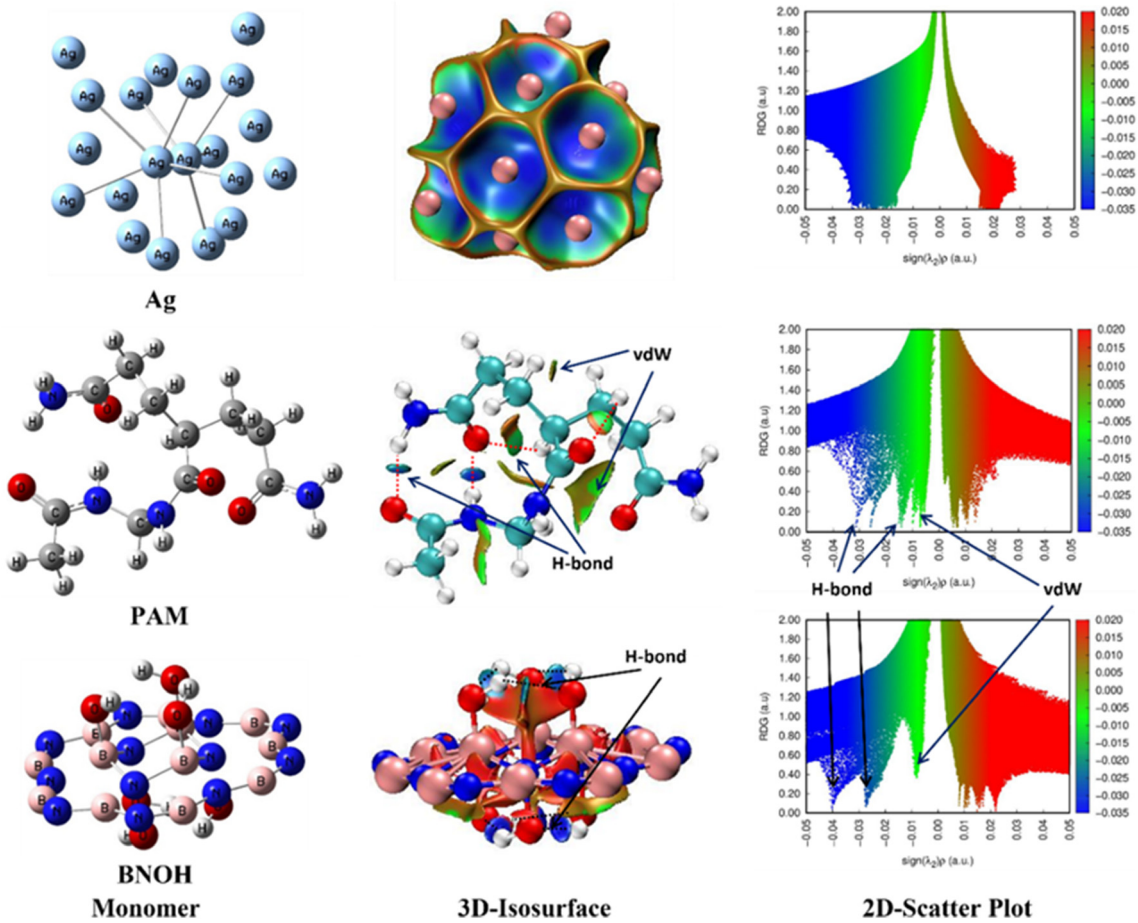

Fig. 14 Optimized/equilibrium structures of the Ag (top-left), PAM (middle-left) and BNOH (below-left) models at the B3LYP/6-31G level of theory along with their respective NCI-plots, 3D-isosurface maps (middle) and 2D-scatter plots (right).

existing above the BN ring and three HBs linked to the N atoms lying below the BN ring) were observed, which self-stabilizes the system (bottom-middle) (HBs shown in black colour dotted line). The B-atom (above the ring)-associated O–H covalent bond distance was calculated as 0.982 Å and the HBDs range from 1.992 Å to 2.001 Å. However, the N-atoms (below the ring) allied O–H CBLs is 1 Å and the HBD range is 1.806 Å–1.811 Å. The QTAIM-based ρ values (0.040 au for two O–H···O HBs and 0.041 au for one O–H···O HB) of the N-associated HBs were observed to be almost 1.5 times greater than those (0.027 for two O–H···O HBs and 0.028 for one O–H···O HB) of the B associated HBs, which clearly demonstrate that the O–H···O HBs located below the BN ring are stronger than the O–H···O HBs lying above the BN ring, as shown in Fig. S5 and Table S2 of the ESI.† Since the B-atoms associated HBs (3D isosurface: three bluish green colour lentils and 2D scatter plot: light blue or bluish-green spikes close to −0.03 au) are weaker than the N-associated HBs (3D isosurface: three dark blue colour discs and 2D scatter plot: dark blue colour spikes close to −0.04 au), which is due to the electronegativity difference between the B and N atoms. A clear picture of two sets (three above and three below) of the HBs, verified from the 3D isosurface map (bottom-middle) and 2D scatter plot (bottom-right) of the NCI plot can be seen in Fig. 14. The other important QTAIM-based parameters; $\nabla^2(\rho)$, V, and DI (A, B) fall in a similar fashion to the electron density (ρ), BPLs, *etc.*

3.2.2. Dimer complex as a composite (two components) model. An *in silico* and in-depth study on the structural, stability/energetics, interfacial interaction(s), and electronic feature analyses of the dimer and trimer (composite models) has been illustrated in this research work. Two composite models in dimer form (PAM-Ag and PAM-BNOH) were selected for the frequency calculations followed by optimization (energy minimization/equilibrium). The first interfacial interactions between the PAM and Ag monomer units have been considered for the PAM-Ag composite model whereas the second interfacial interactions between the PAM and BNOH constituents have been pondered for the PAM-BNOH dimer complex. The optimized structures and parameters of both dimer composite models can be seen in Fig. 15 (top: PAM-BNOH and bottom: PAM-Ag) and Table 3, respectively. The PAM hydrogel model in association with the BNOH (*i.e.* PAM-BNOH) is stabilized by a range of intermolecular NCIs where the PAM unit is self-stabilized

Table 3 Some chosen and useful structural (metal-nonmetal and H-bonded) and other parameters of the three-component models (PAM, Ag, and BNOH) and three composite models (PAM-Ag, PAM-BNOH, and PAM-Ag-BNOH) at the B3LYP/6-31G level of theory

Composite model		
Dimer complex		Trimer complex
PAM-Ag	PAM-BNOH	PAM-Ag-BNOH
Metal–nonmetal bond	Covalent bond between the two components	Metal-nonmetal bond in the PAM-Ag fragment
Ag47–O32 (2.362 Å)	B1-O53 (1.564 Å)	Ag81–O38 (2.398 Å)
Ag46–O27 (2.411 Å)	(Covalent bond, H-bond, bond angle) between the two components	Ag83–H55 (3.168 Å)
Ag45–O17 (2.554 Å)	O31–H32···O63 (0.995 Å, 1.710 Å, 174.1°)	Covalent bond between the two components of the PAM-BNOH fragment
Ag45–H25 (2.751 Å)	O25–H26···O68 (0.977 Å, 1.924 Å, 136.1°)	B1–O53 (1.558 Å)
Ag58–H34 (3.222 Å)	C49–H51···O25 (1.098 Å, 2.087 Å, 176.7°)	(Covalent bond, H-bond, bond angle) between the two components of PAM-BNOH fragment
Ag47–N18 (3.706 Å)	C57–H58···N13 (1.1 Å, 2.135 Å, 151.1°)	O31–H32···O63 (0.994 Å, 1.722 Å, 174.3°)
	N60–H61···O25 (1.019 Å, 2.520 Å, 169.3°)	O25–H26···O68 (0.977 Å, 1.912 Å, 136.4°)
	C49–H51···N15 (1.098 Å, 2.603 Å, 124.7°)	C49–H51···O25 (1.097 Å, 2.079 Å, 170°)
	C41–H43···O25 (1.089 Å, 2.792 Å, 143.8)	C57–H58···N13 (1.1 Å, 2.079 Å, 151.3°)
	Nonconventional bond	N60–H61···O25 (1.019 Å, 2.500 Å, 168.9°)
	O68···O31 (3.187 Å)	C49–H51···N15 (1.097 Å, 2.594 Å, 124.1°)
	N60···N13 (3.401 Å)	C41–H43···O25 (1.089 Å, 2.787 Å, 144.4°)
		Nonconventional bond between the two components of PAM-BNOH fragment
		O68···O31 (3.142 Å)
Component (monomer)		
PAM	Ag	BNOH
N–H bond of NH group (1.025 Å, 1.013 Å)	Bond lengths with respect to two front and central Ag atoms (2.796 Å–3.172 Å)	Outside B–N large ring (1.295 Å–1.398 Å)
N–H bond of NH_2 group (1.007 Å–1.024 Å)		Inside B–N small ring (1.600 Å–1.605 Å)
H-bonded ∠NHO (144.7°, 157.3°)		O–H covalent and H-bond with B atom (0.982 Å, 1.992 Å–2.001 Å)
		O–H covalent and H-bond with N atom (1.000 Å, 1.806 Å–1.811 Å)

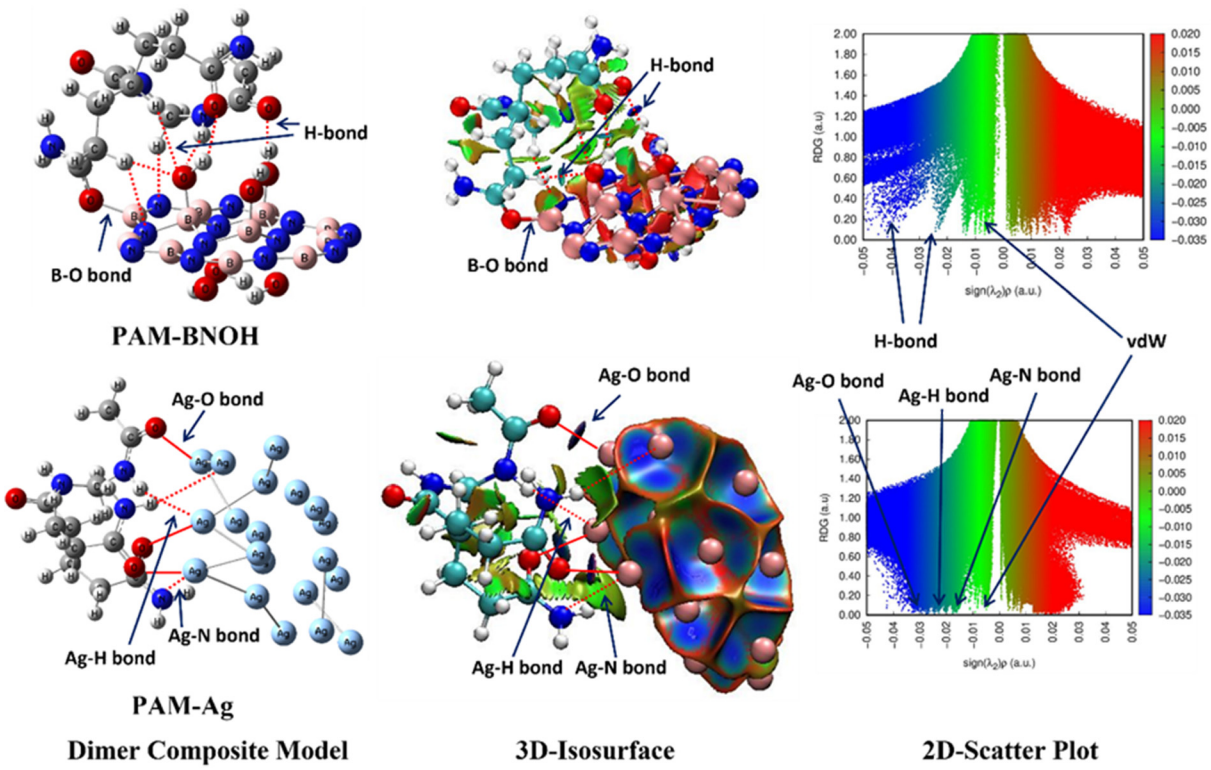

Fig. 15 Optimized/equilibrium structures (left), 3D-isosurafces (middle), and 2D-scatter plots (right) of the PAM-BNOH (top) and PAM-Ag (bottom) dimer complexes (composite models) at the B3LYP/6-31G level of theory.

due to the existence of some intramolecular NCIs (HBs such as N–H···O and C–H···O and extremely weak vdW interactions).

3.2.2.1. Structural feature analysis. A few important and comparable structural parameters related to the covalent bond (B–O), MNIs (Ag–O, Ag–N, and Ag···H), NCIs (weak to moderate HBs), and NBPs for the dimer and trimer composite models were analyzed. For instance, the CBL, HBD, and bond angles of the D–H···A (D → proton donor and A → proton acceptor) fragment and the NBP distance of the composite models are given in Table 3. Keeping in mind the experimental facets and to attain maximum number of bonding and nonbonding interfacial interactions between the two components (PAM and Ag of the PAM-Ag as well as the PAM and BNOH of the PAM-BNOH dimer complexes), a cautious fine-tuning was done in the structures of the three starting materials (monomer units) that showed a minima in the potential energy surfaces.

Having a look into the PAM-BNOH dimer composite model, a total of three kinds of interfacial interactions between the PAM and BNOH components can be discerned. The first type is the covalent bond-one B–O bond (the strongest); the second kind is the NCIs (weak to moderate HBs)-a total of seven H-bonding interactions, namely two O–H···O, one N–H···O, two C–H···O, and two C–H···N HBs; and the third type is the NBP-a total of two NBPs (one O···O and one N···N) were acquired from the QTAIM approach. The B–O covalent bond consists of its respective CBL and BPL as 1.564 Å and 1.568 Å, illustrating the strongest interfacial bonding among all ten interactions. The H-bonded structural parameters of two consecutive O–H···O bonds are (CBL: 0.995 Å and 0.977 Å, HBD: 1.710 Å and 1.924 Å, ∠OHO: 174.1° and 136.1°) consistent with their QTAIM-based corresponding BPL parameters (1.738 Å and 1.950 Å). Having a view into the HBDs and the bond angle, one can see that the former O–H···O HB was observed to be stronger than the latter one (*vide-infra*). Similarly, the other H-bonded structural parameters such as the CBL, HBD, bond angle for the five HBs (one N–H···O and two C–H···O, and two C–H···N) and two NBPs (O···O and N···N) for the PAM-BNOH model can be seen from the earlier mentioned data (Table 3 having the CBL, HBD, bond angle) and Table S3 of the ESI† (showing the BPL values). Surprisingly and interestingly, the BL and BPL of the O···O NBP (3.187, 3.202) are found to be smaller than those (3.401, 4.002) of the N···N NBP; however, the strengths appeared to be the same in terms of the *V* value. The geometrical parameters show that all ten interfacial interactions play an important role in stabilizing the PAM-BNOH composite model.

The dimer composite model PAM-Ag shows a total of six interfacial interactions acting as MNIs (three Ag–O, two Ag···H, and one Ag···N), where the Ag atoms belong to the Ag unit and the O, N, and H atoms are the parts of the PAM component. Out of these six MNIs, the former one (three Ag–O) plays a primary role in stabilizing the dimer composite model, which was affirmed by the QTAIM and NCI-plot tools (*vide-infra*). The bond distances of all the Ag–O bonds were calculated as 2.362 Å, 2.411 Å, and 2.554 Å and the existence of such bonds was supported by the QTAIM tool showing their bond paths (BPLs) (2.365 Å, 2.415 Å, and 2.557 Å, respectively). The QTAIM parameters unravelled that all three probed Ag–O MNIs were found to be stronger than the two Ag···H and one Ag···N MNIs. The (BL, BPL) of the two Ag···H MNIs were detected to be (2.751 Å, 2.780 Å) and (3.222 Å, 3.303 Å) along with one Ag···N MNI (3.706 Å, 3.713 Å).

3.2.2.2. Energetic feature analysis. A few chosen and important energetic-properties fundamental parameters such as binding energy (BE)/interaction energy (IE), energy of the highest occupied molecular orbital (HOMO) and lowest unoccupied molecular orbital (LUMO) and their difference as HOMO–LUMO gap (referred as E_{gap}) are shown in Table 4. To attain new visions into the stability pattern through interfacial (atomic-atomic) interaction(s), the BE/IE parameter was calculated using the supramolecular approach. The IE values for both composite models PAM-Ag and PAM-BNOH were analysed as −18.1 kJ mol^{-1} and −182.9 kJ mol^{-1}, respectively, where the IE of the latter one (PAM-BNOH) is observed to be almost ten times larger than the former one (PAM-Ag). Very importantly and notably, the high stability of the PAM-BNOH is possible due to the presence of a strong (B–O covalent bond) interfacial interaction along with a few weak (C–H···O and C–H···N HBs) to moderate (O–H···O and N–H···O HBs) to taking part therein, as shown in Fig. 15, for which a meticulous rationale for the same was affirmed by the NCI-plots, 3D-isosurface map (top-middle), 2D-scatter plot (top-right) and the QTAIM-based technique (see Fig. S6 of the ESI†) (*vide-infra*).

However, extremely weak (Ag···H and Ag···N) to moderate (Ag–O) interfacial interactions as MNIs in the PAM-Ag can be seen in Fig. 15, which were scrupulously validated by the NCI-plots like the 3D-isosurface map (bottom-middle), 2D-scatter

Table 4 Some selected and important electronic parameters of the three-component models (PAM, Ag, and BNOH) and three composite models (PAM-Ag-BNOH) at the B3LYP/6-31G level of approach

System	PAM-Ag	PAM-BNOH	PAM-Ag-BNOH
Binding energy	−18.1 kJ mol^{-1}	−182.9 kJ mol^{-1}	−218.8 kJ mol^{-1}
HOMO	−4.139	−6.106	−4.648
LUMO	−2.634	−2.090	−2.963
HOMO–LUMO gap	1.505	4.016	1.685
Dipole moment (in Debye, D)	12.1	14.5	13.7
Natural charge	PAM (0.34) Ag (−0.34)	PAM (0.37) BNOH (−0.37)	PAM (0.53) Ag (−0.18) BNOH (−0.35)

plot (bottom-right), and QTAIM molecular graph (see Fig. S7 of the ESI†) (*vide-infra*). Such findings in the PAM-Ag composite model could be due to no significant (less extent of atomic-atomic) interaction(s) between the Ag atoms of the Ag unit (d-orbital of the Ag atom consisting of large size) and the atoms (O, N, and H) of the PAM (s-orbital of the H atom and p-orbitals of the O and N atoms having small size). The QTAIM-based parameters in quantifying the MNIs are tabulated in Table S4 of the ESI† (*vide-infra*). Such outcomes firmly favour the PAM-BNOH composite model (dimer complex) showing its higher stability in comparison to the PAM-Ag moiety.

3.2.2.3. NCI-RDG plot and QTAIM molecular graph. In gaining enhanced understanding and new insights further into the stability and interfacial (bonding and nonbonding) interactions, the NCI-plot and QTAIM tools were deployed for both composite models (PAN-BNOH and PAM-Ag). The NCI-plots (3D isosurface map, 2D scatter plot) of PAM-BNOH (top-middle, top-right) and PAM-Ag (bottom-middle, bottom-right) are displayed in Fig. 15. All interfacial interactions involved in the dimer composites are shown in black colour (B–O bond in solid line and HBs as well as NBPs in dotted line), where BCPs are shown by big sphere (in light blue colour). Taking PAM-BNOH as the first example, a total of eight stabilizing interfacial interactions as the conventional bond paths (a strong B–O covalent bond and seven HBs such as two O–H···O, one N–H···O, two C–H···O, and two C–H···N) and two NBPs (O···O and N···N) were detected using both the above-discussed tools. The QTAIM tool shows that a bonding (B–O) interaction (shown in solid line) is observed for which ρ and $\nabla^2(\rho)$ values are computed as 0.107 au (order of 10^{-1} au) and +0.404 au, respectively, indicating the strongest bonding interaction among all ten interfacial interactions. Such values are also supported by the geometrical parameters (BL: 1.564 Å and BPL: 1.568 Å), showing the smallest BL and BPL among all interactions involved in the PAM-BNOH.

The evidence of the presence of the strong B–O interfacial bonding interaction is shown by both the 3D isosurface map (shown in solid line) and 2D scatter plot (dark blue colour with broader spikes ranging between −0.04 au and −0.05 au). Similarly, the NCI-plot (top-middle and right of Fig. 15) and QTAIM (Fig. S6 of the ESI†) techniques exposed the presence of seven HBs. For instance, the QTAIM parameters [ρ, $\nabla^2(\rho)$] decreased (0.045 au, +0.0148 au → 0.024 au, +0.101 au) for the O–H···O HBs as the corresponding H-bonded geometrical parameters (HBD, BPL) increased (1.710 Å, 1.738 Å → 1.924 Å, 1.950 Å) and the bond angle decreased (174.1° → 136.1°). The sign of the existence of the all-interfacial interactions *via* the HBs in the PAM-BNOH is further validated by the 3D isosurface map (strong HB: dark blue; moderate/weak HB: bluish-green/dark green lentils) and 2D scatter plot (strong HB by dark blue and moderate/weak HBs by bluish-green/dark green colour peaks ranging between −0.015 au and −0.04 au), as displayed in Fig. 15. The QTAIM topological parameters for other interfacial interactions (HBs) like the one N–H···O, two C–H···O, and two C–H···N are consistent with the H-bonded geometry-based parameters (Table S3 of the ESI†). Extremely weak vdW interactions and NBPs between two interfaces of the PAM and BNOH components are demonstrated in a bright green colour scheme (peaks of the 2D Scatter plot ranging from 0 to −0.01 au). One can note that one of the important local potential energy density (V) parameters (one of the main quantifying stabilizing parameters) also gives a similar trend in all H-bonding cases.

On investigating the interfacial interactions in the PAM-Ag composite model (dimer complex), a total of six interfacial interactions as the MNIs (three Ag–O, two Ag···H, and one Ag···N) were detected, which were further confirmed by the NCI-plot (bottom-middle and right) and the QTAIM (Table S4 and Fig. S7 of the ESI†) tools. Three moderate Ag–O metal-non-metal bonds shown in a solid line in red colour scheme (bottom-left and middle) can be seen in the 2D scatter plot (bottom-right) (blue colour spikes ranging between −0.025 au and −0.04 au), which were further validated by the 3D isosurface map diagram (see three blue colour lentils in the bottom-middle). The QTAIM parameters [ρ, $\nabla^2(\rho)$] have been calculated as (0.043, +0.227), (0.039, +0.197), and (0.030, +0.133) (in au) for all three Ag–O MNIs and there is good consistency with their corresponding structural MNI related parameters (BL, BPL) (2.362 Å, 2.365 Å), (2.411 Å, 2.415 Å), and (2.554 Å, 2.557 Å) (Table S4 of the ESI†). The respective local potential energy density (V) values strongly favour the above-discussed parameters. Importantly, three weak MNIs (two Ag···H and one Ag···N), responsible for stabilizing the PAM-Ag composite model, were assured by the same analyses and tools for which the data and diagram are shown in Table S4 and Fig. S7 of the ESI.† The light or bluish-green colour peaks ranging from −0.015 au to −0.025 au as exposed in the 2D scatter plot show the existence of the weak to moderate Ag···H and Ag···N bonds, whereas the extremely weak vdW interactions are represented in bright green colour spikes ranging between 0 and −0.01 au. The 3D isosurface maps also express the existence of such MNIs along with illustrating the vdW interactions. Since, having a quick view into both composite models (dimer complexes), it is found that PAM-BNOH is more stable than PAM-Ag, which is because of the involvement of stronger interfacial interactions in the former one (*vide-infra*).

3.2.3. Trimer complex as a composite (three components) model. In this work, very interestingly and importantly taking care of the experimental facets, a trimer composite model (PAM-Ag-BNOH was assembled using a 3D three-body with two-sided interfacial interactions: one between the PAM and Ag components and the other between the PAM and BNOH components) followed by the molecular modelling approach is reported. In order to get new insights and understand the binding features (*i.e.* interfacial interactions) in the PAM-Ag-BNOH composition, the QTAIM tool facilitated a total of four kinds of interfacial interactions (first type – one interface side of the PAM-Ag dimer constituent and the second, third and fourth type – another interface side of the PAM-BNOH dimer segment). The first kind of interfacial interaction, two MNIs (Ag–O and Ag···H) between the PAM unit and Ag assembly of

the PAM-Ag fragment, is responsible for moderately binding both the components together. The distance and the QTAIM-based BPL between interacting Ag and O atoms of Ag–O are detected to be 2.398 Å and 2.401 Å, correspondingly; however, the respective distance and BPL of Ag–H MNI are 3.168 Å and 3.240 Å, which moderately embrace the PAM and Ag assembly and stabilize the one side interface.

The second type of interfacial interaction is the B–O (covalent bond) interaction (CBL: 1.558 Å; BPL: 1.562 Å) between the O atom of the PAM and the B atom of the BNOH (very tightly holds both the PAM and BNOH together) and strongly reinforces the interfacial interactions occurring on the other side. The B–O bond distance speaks well that it was the strongest binding interaction among all bonding and non-bonding interactions participating in the PAM-Ag-BNOH trimer composite model. As discussed earlier in the previous paragraph, a similar case of the first type of interfacial interaction (B–O covalent bonding interaction) was also detected in the case of the PAM-Ag dimer composite. Now, the third kind of interfacial interactions (*i.e.* NCIs) participating in the PAM-Ag-BNOH model is also the second type of interfacial interactions that took part in the PAM-BNOH dimer composite. Like PAM-BNOH species, a total of seven NCIs (weak to moderate HBs); two O–H···O, one, N–H···O two C–H···O, and two C–H···N were found between the binding sites of the PAM and BNOH components of the PAM-Ag-BNOH composite. The structural parameters (HBD, BPL, bond angle) of both O–H···O bonds in the trimer complex have been analyzed as (1.722 Å, 1.750 Å, 174.3°) and (1.912 Å, 1.978 Å, 136.4°) where the former one O–H···O HBD is increased by 0.012 Å and the latter one O–H···O HBD is decreased by 0.012 Å when comparing these with the PAM-BNOH dimer complex (see Table 3). These structural changes clearly illustrate that the strength of the former O–H···O interaction is reduced whereas the latter one is enhanced which was confirmed by the QTAIM-based topological parameters (see Table S3 for the PAM-BNOH and S5 for the PAM-Ag-BNOH of the ESI†) and supported by the structure/geometry-based H-bond strength quantifying criteria (Fig. 16). Several observations for the other two NCIs (C–H···O and C–H···N) can be seen from the same Tables. Furthermore, only one NBP (one O···O) was found in the case of the trimer composite while there were two NBPs (one O···O and one N···N) in the case of the PAM-BNOH dimer complex which could be due to modification in the orientation of the com-

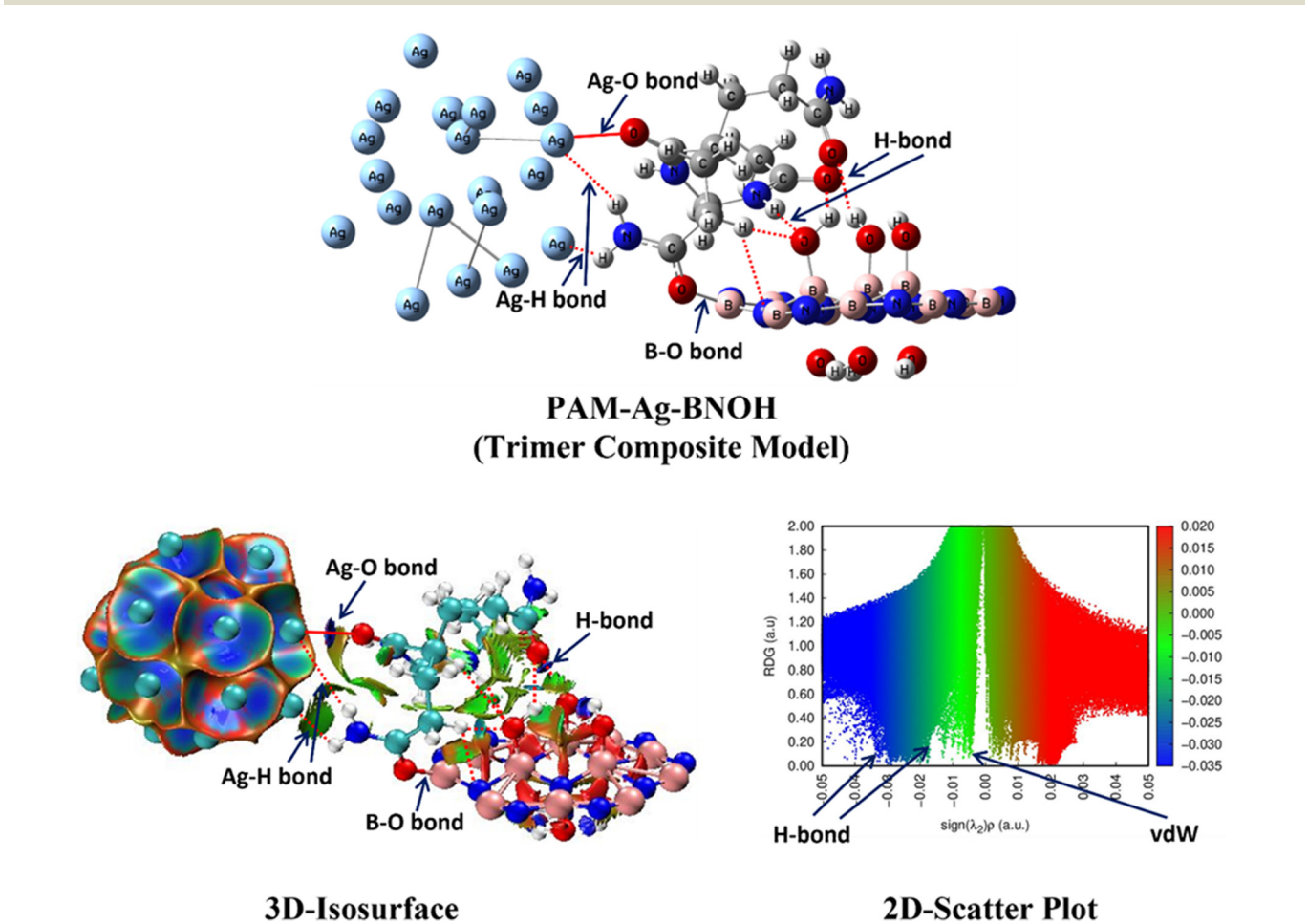

Fig. 16 Optimized/equilibrium structures (top), 3D-isosurafces (left), and 2D-scatter plots (right) of the PAM-Ag-BNOH trimer complex (composite model) at the B3LYP/6-31G level of theory.

ponents in order to make minimum energy (optimized/equilibrium) structure. It is important to mention that such findings were strongly promoted from the NCI-plot as well as the QTAIM tool since the structural parameters demonstrate the most stability of the trimer composite model among all the three.

3.2.3.1. Energetic feature analysis. Now, having a closer view into the IE parameter of the trimer composite model (PAM-Ag-BNOH) which consists of two different interfacial actions (one between the PAM and Ag and the other between the PAM and BNOH), the calculated BE/IE value (−218.8 kJ mol^{-1}) is the highest among all the three composites (PAM-Ag and PAM-BNOH dimer and PAM-Ag-BNOH trimer composite models) as expected. Moreover, such bonding (*i.e.* BE/IE) in the trimer (PAM-Ag-BNOH) composite model (−218.8 kJ mol^{-1}) is almost twelve times greater than that in the dimer (PAM-Ag) composite model (−18.1 kJ mol^{-1}) and clearly demonstrates that the former one is the most stable among all three composite models. There is an extra stability (−17.8 kJ mol^{-1}) in the trimer case, which comes due to the blending of the PAM unit to both other components (Ag and BNOH). The extra stability is the difference between the IE value (−218.8 kJ mol^{-1}) of the PAM-Ag-BNOH and the sum of the IE (−201 kJ mol^{-1}) of both dimer composite models (−18.1 kJ mol^{-1} for the PAM-Ag and −182.9 kJ mol^{-1} and PAM-BNOH). Conclusively, by scanning all these three analysed BE/IE parameters, the trimer composite model appeared to be the most stable species, which favoured the experimental facet-based outcomes like the largest value of the compressive strength (0.31 MPa) and Young's modulus (0.29 MPa) values of the PAM blended with the Ag as well as BNOH components together (PAM-Ag-BNOH composite). Notably, the order of BE/IE (*i.e.* a theory-based analyzed stability parameter) is Ag-BNOH (−218.8) > PAM-BNOH (−182.9) > PAM-Ag (−18.1) (in kJ mol^{-1}), which is consistent with two experimentally detected (mechanical strength) parameters (compressive strength and Young's modulus), illustrating the same order as PAM-Ag-BNOH (0.31, 0.29) > PAM-BNOH (0.26, 0.27) > PAM-Ag (0.22, 0.21) (in MPa). Such outcomes regarding the above inspected order are also verified and then supported by the charge transfer (CT) feature analyses using the natural population analyses (NPA) tool (*vide-infra*).

3.2.3.2. NCI-RDG plot and QTAIM molecular graph. Lastly, Fig. 16 shows the interfacial (bonding and nonbonding) interactions for two interfaces (one between the PAM and Ag units and the other between the PAM and BNOH components), as examined in the optimized PAM-Ag-BNOH composite model (trimer complex). The QTAIM outcomes (Fig. S8 and Table S5 of the ESI†) facilitate a clear portrait of both types of interfacial interactions. In the case of the first kind of interfacial interactions, two BCPs (bridged between the PAM and Ag components) are illustrated as one Ag–O and one Ag···H MNI. In addition, nine BCPs (one B–O bond, seven HBs, and one NBP between the PAM and BNOH units) are shown for the second type of interfacial interaction. The first interface is constructed between the Ag and PAM units of the dimer fragment (PAM-Ag) of the trimer complex (PAM-Ag-BNOH). The interaction estimating parameters [ρ, $\nabla^2(\rho)$] for Ag–O MNI were analyzed as (0.040 au, +0.205 au) while these values for Ag···H MNI were observed to be (0.005 au, +0.012 au). Importantly, the electron density, ρ, value of the former one (0.040 au) is detected to be eight times larger than the latter one (0.005 au), which is in accordance with their respective geometrical criteria [Ag–O bond: (BL: 2.398 Å, BPL: 2.401 Å); Ag···H bond: (BL: 3.168 Å, BPL: 3.240 Å)] as well as the other QTAIM-based local potential energy density and delocalization index parameters. Like the QTAIM tool, the Ag–O and Ag···H types of the MNIs are also supported by an NCI-plot technique (3D isosurface and 2D scatter plot). The presence of moderate Ag–O bond (spikes range between −0.030 au and −0.04 au) and weak Ag···H MNI (peaks range from −0.01 au to −0.02 au) is favoured by the peaks (moderate Ag–O: blue and weak Ag–H: light blue) observed in the 2D scatter plot. The existence of the Ag–O bond is also shown by the blue colour lentil in the 3D isosurface map, whereas the bluish-green/dark-green colour lobe shows the presence of the weak Ag···H bond connecting the PAM and Ag constituents.

In the second type of interactions between the PAM and BNOH units of the dimer fragment (PAM-BNOH) of the trimer complex (PAM-Ag-BNOH), among a total of nine interfacial interactions, one strong B–O (stronger than that in PAM-BNOH dimer) and seven HBs (two O–H···O, one N–H···O, two C–H···O, and two C–H···N), and one NBP (O···O) were probed using the QTAIM approach (Fig. S8 of the ESI†). The geometrical parameters (BL, BPL) (1.558 Å, 1.562 Å) for the B–O bond is decreased in the trimer complex, while it (1.564 Å, 1.568 Å) was higher in the dimer case and indicating the presence of strong bonding interaction between the B atom of BNOH component and O atom of the PAM unit. Moreover, the QTAIM-analyzed [ρ, $\nabla^2(\rho)$] values of the B–O bond of the trimer have been computed as (0.109 au, +0.422 au), whereas the same parameters (0.107, +0.404 au) are smaller in the case of the dimer complex. Furthermore, the V value of the trimer composite model (−0.217 au) is marginally greater (0.004 au) than that of the dimer composite (−0.213 au). Next, among the seven HBs, three HBs give the impression of the occurrence of one moderate (O–H···O) to two weak HBs (O–H···O and C–H···O). The computed [ρ, $\nabla^2(\rho)$] values for the moderate *versus* weak O–H···O HBs are (0.043 au, +0.143 au) and (0.025 au, +0.104 au), which are as expected according to the geometry-based criteria (see BL and BPL values for both HBs). The structural parameters and QTAIM-based topological parameters for the rest of the five HBs give additional information about the interfacial interactions and thus play significant roles in stabilizing the trimer complex for the interface between the PAM and BNOH units. In stabilizing the trimer complex, the role of a single O···O NBP (BL: 3.142 Å, BPL: 3.154 Å) having the computed [ρ, $\nabla^2(\rho)$] values as (0.006 au, +0.025 au) also cannot be ignored.

Similarly, the NCI-plot (2D scatter plot) demonstrates the presence of one moderate O–H···O HB (blue peak lying between −0.02 au and −0.03 au) and two weak HBs (one O–

H···O and one C–H···O) (bluish-green spikes lying between −0.015 au and −0.02 au), which can be verified by the 3D isosurface map (blue lentil for the moderate HB and bluish-green discs for weak HBs). The rest (four) of the HBs (one C–H···O, one N–H···O, and two C–H···N) are found to be extremely weak, which were inspected by the QTAIM as well as the NCI-plot approaches. The 2D scatter map (green colour band range from 0 to −0.015 au) and 3D isosurface map (green colour discs) provide another proof of the occurrence of the extremely weak HBs. Some vdW interactions between the Ag and PAM unit as well as between the BNOH and PAM components play primary roles as supplementary sites in stabilizing the composite model based on three components (trimer complex).

3.2.3.3. Frontier molecular orbitals (FMOs) of the dimer and trimer composite models. The HOMOs and LUMOs are usually labelled as the Frontier molecular orbitals (FMOs) in the FMO theory. Chemical behaviours such as strength and stability (reciprocal to the chemical reactivity) of any chemical moiety can be predicted by using the difference of the HOMO and LUMO parameters (E_{gap}) of the FMOs.[75] The electron donating and accepting capabilities of a molecular entity are directly related to the E_{HOMO} and E_{LUMO} parameters, correspondingly, difference of the HOMO and LUMO parameters (E_{gap}) indicates the global chemical hardness. In this report. A few interesting and important electronic features such as the HOMOs, LUMOs, E_{gap}, chemical hardness, dipole moment, HOMO–LUMO plots of the dimer and trimer composite models are displayed in Table 4. The order of three parameters (HOMO, E_{gap}, and dipole moment) for all three entities (two dimer and one trimer) follow the same trend as PAM-BN (−6.106 eV, 4.016 eV, 14.5 D) > PAM-Ag-BNOH (−4.648 eV, 1.685 eV, 13.7 D) > PAM-Ag (−4.139 eV, 1.505 eV, 12.1 D), indicating that PAM-BNOH is chemically less reactive (more stable) than the other two. This highlighted that a higher HOMO value (for example, −6.106 for the PAM-BNOH) means the system has a good electron donating feature. However, the order of the LUMOs is computed as PAM-Ag-BNOH (2.963 eV) > PAM-Ag (−2. 634 eV) > PAM-BNOH (−2.090 eV), illustrating the highest electron accepting tendency of the trimer composite model among all three.

The three-dimensional (3D) isosurface maps of the HOMOs and LUMOs of all three examined models are displayed in Fig. 17. In the case of the PAM-Ag system (see left), the HOMOs (bottom-left) are primarily localized over five terminal Ag atoms (in-phase) of the Ag assembly; however, a small contribution from the rest of the Ag atoms can also be seen in the HOMO 3D-isosurface. However, the LUMOs (top-left) are mainly confined to six Ag atoms (a few are out-phase) along with minor distribution on the rest of the Ag atoms. Such observation shows that Ag atoms of the Ag cluster (component) play a primary role in the PAM-Ag composite during the electronic transitions. The HOMOs of PAM-BNOH (bottom-middle) are majorly spread over some B–N fragments of the BN rings which are close to the PAM component along with minor contribution on a few OH substituted groups of the BNOH constituent as well as one $CONH_2$ group, one CONH group, and one CH_2 group of the PAM unit. However, the

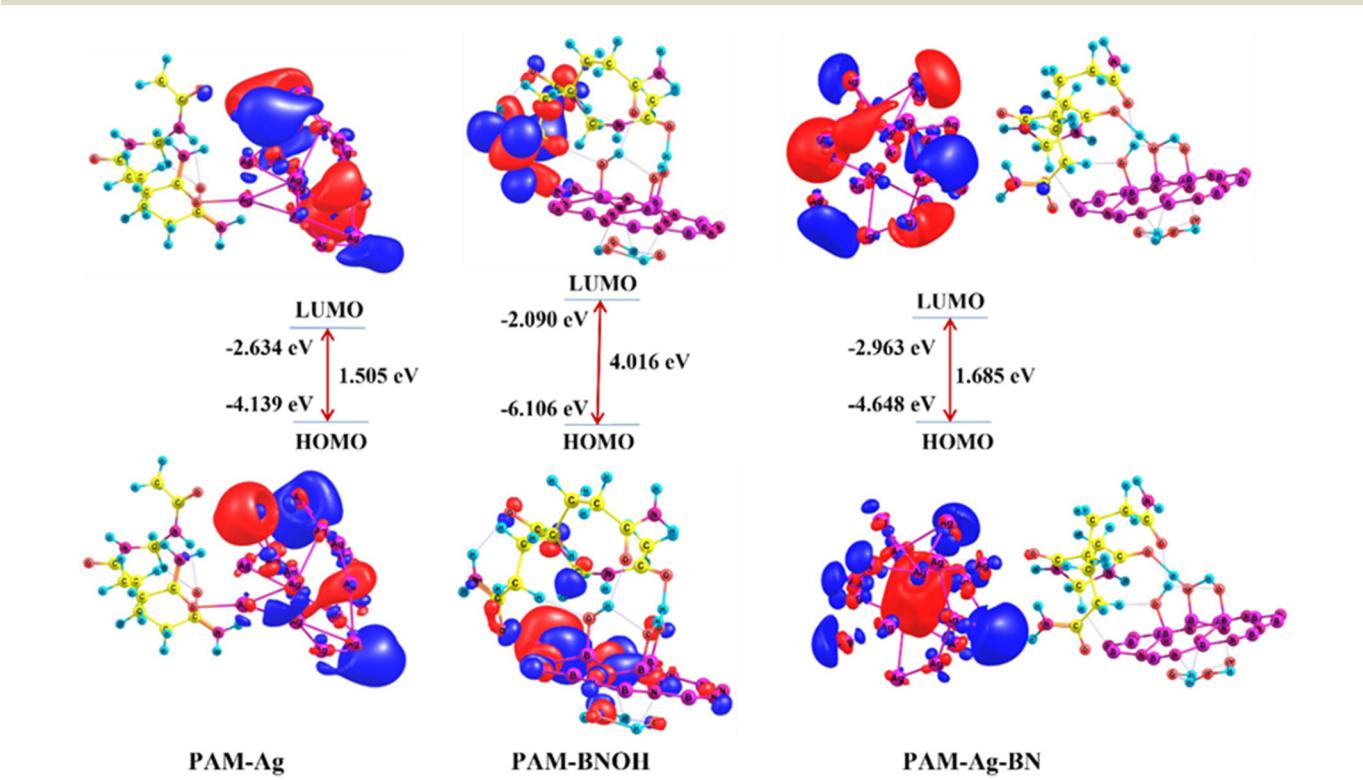

Fig. 17 HOMO and LUMO isosurface maps of the optimized structures of the dimer (PAM-Ag and PAM-BNOH) and trimer (PAM-Ag-BNOH) complexes as composite models at the B3LYP/6-31G level of theory.

LUMOs (top-middle) are delocalized over one CH_2CONH_2 group and the CON bonding region of the PAM unit.

The HOMO–LUMO 3D isosurface maps of the PAM-Ag-BNOH composite model (trimer complex) (see right) demonstrate that the distribution of the HOMOs (bottom-right) can be viewed on one Ag atom (neighbour of the PAM component), four Ag located at the terminals, and one Ag lying at the centre of the Ag assembly. A small contribution of the HOMOs from other Ag atoms of the Ag assembly, O and N atoms of the CON bonding fragment as well as only the N-atom of the $CONH_2$ group of the PAM unit can also be seen, whereas the LUMOs are largely specified over eight Ag atoms (at the terminals) along with a little distribution on the remaining Ag atoms of the Ag cluster, CON fragment of one of the $CONH_2$ groups as well as C atom of one of the CONH segments.

3.2.3.4. Molecular electrostatic potential (MESP) surfaces of the components, dimer and trimer composite models. The molecular size, shape, and atomic charge distribution are directly connected to the electron density as well as the molecular electrostatic potential (MESP). Therefore, to understand the NCIs, electrophilic as well as nucleophilic attack (*i.e.* reactivity nature), relative polarity, and attaining other pathways in the diagnosing of one chemical species by another, the concept of the MESP (through the electron density) has vastly been deployed.[76] The MESP 3D-isosurface maps of the monomer to dimer to trimer models are displayed in Fig. 18. Absolute positive charge distributions (a high possibility of the nucleophilic attack) are spread over the electron-needy (deficient) regions (*i.e.* reactive site) and are presented in a blue colour scheme, where the red colour scheme explains the electrophilic attack regions consisting of electron-rich (excess) regions through absolutely negative charge distribution. Moreover, the neutral region is illustrated by the green colour scheme. In all cases (monomer unit, dimer and trimer composite models), whether terms of entities or components, positive charge regions are distributed over the NH_2 group of PAM and OH group of BNOH along with minor localization on the CH_2 fragment of PAM. The regions (shown in red color) near the O atoms of the carbonyl group (CO) of three moieties (PAM monomer, PAM-Ag and PAM-BNOH) and BNO/NBO segments of BNOH show electron-rich localities. The hybrid color (orange) reveals mild electron-rich regions, which can be viewed in the case of the BNOH rings of the PAM-BNOH and PAM-Ag-BNOH composite models. Interestingly, the environments close to the Ag assembly in the PAM-Ag composite show green color, which indicates neutral regions whereas regions near the PAM component are shown in the bluish-green color scheme. Conversely, in the case of the PAM-Ag-BNOH model, the areas near the Ag assembly are illustrated in a red color scheme and appear to show an electron-rich region, which appears to be

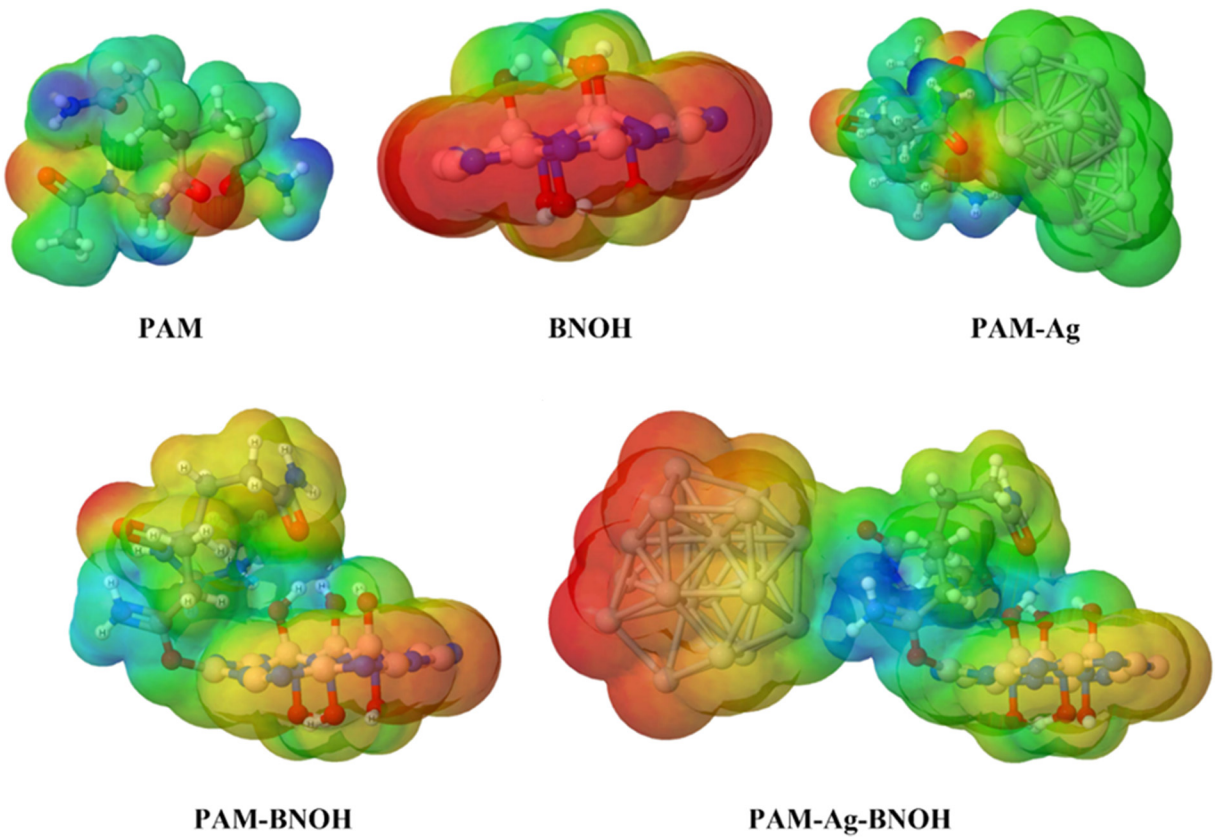

Fig. 18 MESP lots of the monomer (PAM and BNOH) units, dimer (PAM-Ag and PAM-BNOH) and trimer (PAM-Ag-BNOH) complexes as composite models.

due to the existence of excess d-electrons of the Ag atoms. Such findings are strongly supported by the natural population analyses (NPA), which are discussed in the below section.

3.2.3.5. Natural population (atomic charge) assessment of the dimer and trimer composite models. The charge distribution on the nuclei, bond order, and many other interdependent information such as charge transfer (CT) phenomenon can be extracted from the NPA tool, which is helpful in the assessment of the electron (charge) population of every atom of any type of chemical system. Very importantly and notably, one can see that in all three cases of the composite models, the PAM component consists of a positive charge, whereas the Ag and BNOH components contain a negative charge (see Table 4). Taking as the first case of the PAM-Ag dimer composite model, the CT takes place from PAM to Ag assembly, which is due to the allocation of positive charge on the PAM (0.34e) and negative charge on the Ag assembly (−0.19*e*). Now, the NPA technique explains the positive natural charge on the PAM constituent (0.37) and negative natural charge (−0.37) on the BNOH component in the case of the PAM-BNOH composite (dimer complex and portraying the CT occurring from PAM to the BNOH segment). Moreover, in this case, the charge is marginally larger (0.03*e*) than in the PAM-Ag case. Lastly, the trimer composite model (PAM-Ag-BNOH) clarifies that the PAM component has the positive natural charge (0.53*e*) while the other two components, Ag (−0.18*e*) and BNOH (−0.35*e*) units, have the largest negative charges. It is interesting to see that the sum (−0.18*e* to 0.35*e* = −0.53*e*) of the charges (excluding the sign) on the Ag assembly (−0.18*e*) and BNOH (−0.35*e*) component is equal to the charge on the PAM unit (0.53). Therefore, the order of both kinds of charge distributions (positive, negative) for all probed three species is PAM-Ag-BNOH (Q_{PAM} = 0.53 e, $Q_{Ag+BNOH}$ = −0.53*e*) > PAM-BNOH (Q_{PAM} = 0.37*e*, Q_{BNOH} = −0.37*e*) > PAM-Ag (Q_{PAM} = 0.34*e*, Q_{Ag} = −0.34*e*). The highest positive and negative charges on the PAM (0.53*e*) and Ag + BNOH (−0.53*e*) components of the trimer composite suggest that it is the most stable complex among all three composite models which are also favoured by the BE/IE, NCI-plot (3D isosurface maps and 2D scatter plot), and the QTAIM topological parameters along with two experimental findings such as compressive strength and Young's modulus.

Thus, it is clear from the above discussion that the addition of optimum concentration of Ag and BNOH in the PAM matrix can offer amended mechanical strength, long-term durability of the material in SBF (or corrosion resistance), restricted toxicity, good anti-microbial activity along with strong interfacial interactions between reinforced particles and PAM. Fig. 19 is the schematic representation of current research showing that

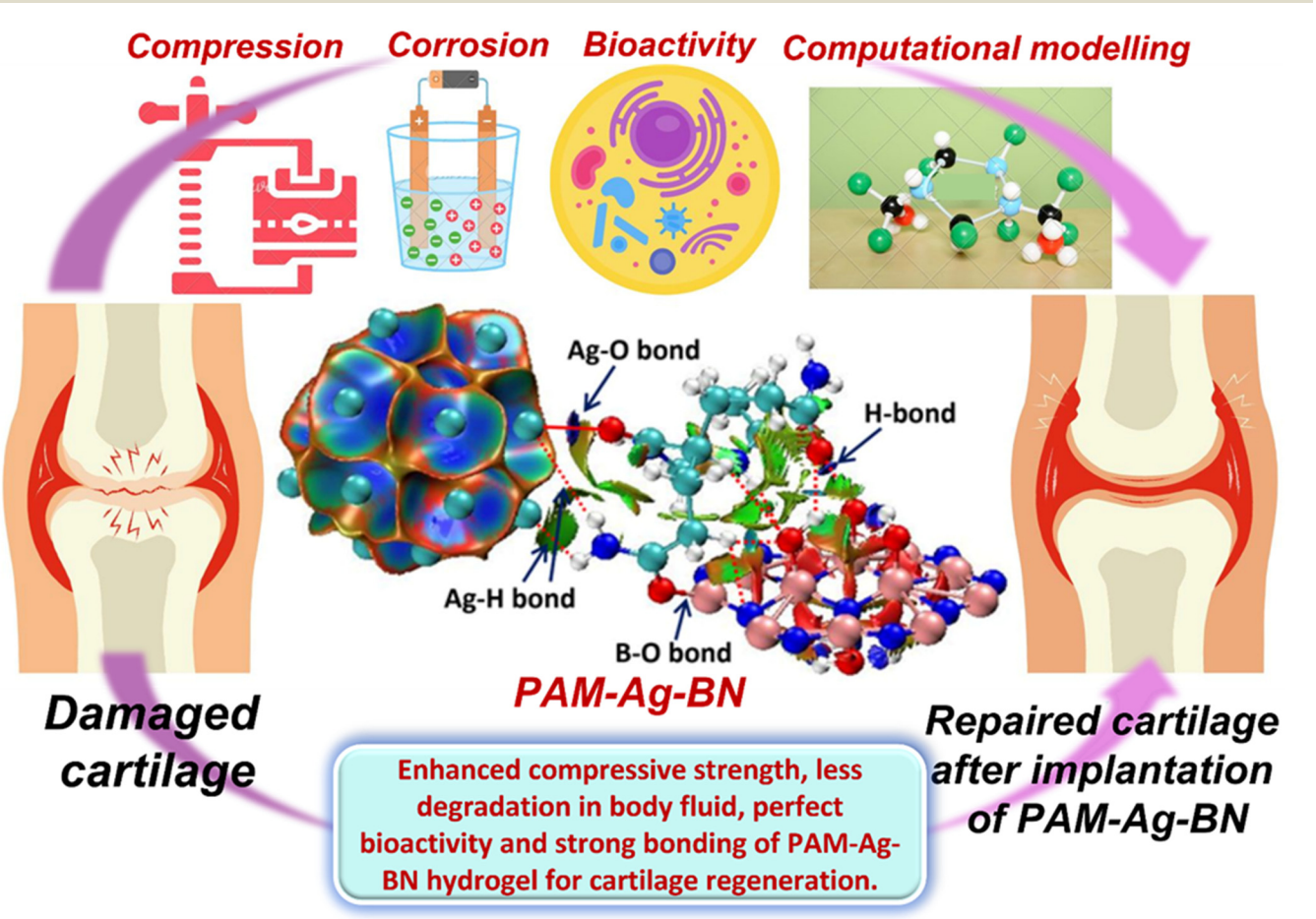

Fig. 19 Schematic of cartilage regeneration by the PAM-Ag-BN hydrogel using various experimental and theoretical studies.

the prepared trimer hydrogel composite PAM-Ag-BN was tested by a compression test, for long-term stability of hydrogel in a simulated body fluid using electrochemical investigations. Moreover, the bioactivity of the material was confirmed by biomineralization, self-healing, cytocompatibility and anti-bacterial activity. The computational experiments supported the wet-lab experiment, and it showed that the Ag assembly and functionalized BN (BNOH) played roles as reactive sites in the PAM-Ag-BNOH composite hydrogel and yielded strong (B–O, H-bond) to moderate (Ag–O, H-bond) to weak (Ag···H, H-bond) NBPs (O···O). The PAM-Ag-BN hydrogel showed high strength, improved stability in SBF, perfect bioactivity and strong bonding, which constructs the PAM-Ag-BN hydrogel as a prime implant for cartilage repair applications (Fig. 19).

4. Conclusions

The reinforcement of Ag and BNOH in the PAM matrix provided new hydrogel composites. The mechanical strength was tested for different concentrations of Ag and BNOH with PAM and it was demonstrated that BN-based hydrogel composites showed higher compressive strength (0.26 MPa) and elastic modulus (0.27 MPa) than that of Ag-based composites. The hexagonal boron nitride used in the fabrication of PAM-BN composites was functionalized with a hydroxyl group and, as a result, the formation of hydrogen bonding occurs between BNOH and PAM. The strong interfacial interlocking of BNOH with PAM delivered strong mechanical properties over Ag. Among all concentrations of Ag and BNOH, 0.1 wt% and 0.3 wt% of Ag and BNOH were recognized as optimum concentrations, respectively. These optimum concentrations were mixed with PAM and a novel trimer composite was developed (PAM-Ag-BN). The electrochemical studies between trimer composite and optimum concentrations of Ag (PAM-Ag1) and BNOH (PAM-BN3) showed improved corrosion resistance for the trimer. The bioactivity of the samples was further investigated by testing bone-forming ability, self-healing, cytotoxicity and antimicrobial activity *in vitro*. The PAM-Ag-BN also showed enhanced biological performance due to the synergistic effect of nano- and micron-sized particles and strong bonding. Moreover, in understanding better and achieving new insights into the structural, stability/energetics, interfacial interaction (s), and electronic features, the computational experiments provide a substantial proof that the interfacial (bonding and nonbonding) interactions between two components are mainly administered by the covalent bonding, metal-nonmetal interactions, H-bonding, and other weak interactions along with the vdW interactions inspected in three composite models (PAM-Ag, PAM-BNOH, and PAM-Ag-BNOH). Good understanding of the binding features of the biocomposites (PAM-Ag, PAM-BNOH, and PAM-Ag-BNOH) is accomplished using the *in silico* technique followed by the molecular modelling approach and DFT studies and since, such examples could overlay pioneering revelation in biomedical applications. Thus, it is concluded that the PAM-Ag-BN hydrogel composite with enhanced mechanical strength, bioactivity and strong bonding can be an advanced hydrogel composite for cartilage repair applications.

Author's response

It is stated that all the images/artwork/photos that appear in this manuscript and ESI,† including the TOC graphic, were created/taken by the authors of this manuscript.

Author contributions

Shikha Awasthi: writing – original draft, writing – review and editing, investigation, and supervision conceptualization. Sarvesh Kumar Pandey: writing – review and editing, visualization, investigation, and conceptualization. Hulikere Jagdish Shwetha: methodology and formal analysis. Nehal: methodology and formal analysis. S. Selvaraj: methodology and formal analysis.

Data availability

Data will be made available on request.

Conflicts of interest

There are no conflicts to declare.

Acknowledgements

S. A. thanks to the Department of Chemistry Manipal University Jaipur, Central Analytical Facility, Manipal University Jaipur for providing elemental mapping facilities and the Department of Science and Technology (DST) Rajasthan, India for providing a research grant (13(186)/2024-25/2603). S. K. P. is thankful to the MANIT, Bhopal for facilitating a research seed grant (RSG) to perform the research work and also thanks IIT Kanpur, India for providing the computational facilities. SA is also thankful to Professor A. Raichur, IISc Bangalore for providing bioactivity testing.

References

1 L. Montero De Espinosa, W. Meesorn, D. Moatsou and C. Weder, *Chem. Rev.*, 2017, **117**, 12851–12892.
2 J. P. Gong, Y. Katsuyama, T. Kurokawa and Y. Osada, *Adv. Mater.*, 2003, **15**, 1155–1158.
3 J. Y. Sun, X. Zhao, W. R. K. Illeperuma, O. Chaudhuri, K. H. Oh, D. J. Mooney, J. J. Vlassak and Z. Suo, *Nature*, 2012, **489**, 133–136.
4 B. Choi, S. Kim, B. Lin, B. M. Wu and M. Lee, *ACS Appl. Mater. Interfaces*, 2014, **6**, 20110–20121.

5 N. A. Peppas, J. Z. Hilt, A. Khademhosseini and R. Langer, *Adv. Mater.*, 2006, **18**, 1345–1360.
6 F. Yokoyama, I. Masada, K. Shimamura, T. Ikawa and K. Monobe, *Colloid Polym. Sci.*, 1986, **264**, 595–601.
7 D. A. Sánchez-Téllez, L. Téllez-Jurado and L. M. Rodríguez-Lorenzo, *Polymers*, 2017, **9**, 1–32.
8 S. Awasthi, *JOM*, 2021, **73**, 2440–2451.
9 S. Awasthi, *Mater. Today Chem.*, 2024, **35**, 101877.
10 S. Awasthi and S. K. Pandey, *Appl. Mater. Today*, 2024, **36**, 102058.
11 A. Tangri, *Int. J. Pharm., Chem. Biol. Sci.*, 2014, **4**, 951–959.
12 D. Olpan, S. Duran and O. Güven, *J. Appl. Polym. Sci.*, 2002, **86**, 3570–3580.
13 M. R. Guilherme, A. V. Reis, S. H. Takahashi, A. F. Rubira, J. P. A. Feitosa and E. C. Muniz, *Carbohydr. Polym.*, 2005, **61**, 464–471.
14 C. Mihăilescu, A. Dumitrescu, B. C. Simionescu and V. Bulacovschi, *Rev. Roum. Chim.*, 2007, **52**, 1071–1076.
15 S. K. Bajpai and S. Dubey, *Iran. Polym. J. (Engl. Ed.)*, 2004, **13**, 189–203.
16 S. N. Li, B. Li, L. X. Gong, Z. R. Yu, Y. Feng, D. Jia, Y. Zhou and L. C. Tang, *Mater. Des.*, 2019, **162**, 162–170.
17 R. Parhi, *Adv. Pharm. Bull.*, 2017, **7**, 515–530.
18 S. Gurunathan, K. J. Lee, K. Kalishwaralal, S. Sheikpranbabu, R. Vaidyanathan and S. H. Eom, *Biomaterials*, 2009, **30**, 6341–6350.
19 M. Guzman, J. Dille and S. Godet, *Nanomedicine*, 2012, **8**, 37–45.
20 P. L. Nadworny, J. F. Wang, E. E. Tredget and R. E. Burrell, *Nanomedicine*, 2008, **4**, 241–251.
21 K. Kalishwaralal, S. BarathManiKanth, S. R. K. Pandian, V. Deepak and S. Gurunathan, *Colloids Surf., B*, 2010, **79**, 340–344.
22 E. Olăreț, Ș. I. Voicu, R. Oprea, F. Miculescu, L. Butac, I. C. Stancu and A. Serafim, *Polymers*, 2022, **14**, 2320.
23 M. I. González-Sánchez, S. Perni, G. Tommasi, N. G. Morris, K. Hawkins, E. López-Cabarcos and P. Prokopovich, *Mater. Sci. Eng. B*, 2015, **50**, 332–340.
24 D. M. Lima, A. C. Chinellato and M. Champeau, *Soft Matter*, 2021, **17**, 4475–4488.
25 X. Hu, J. Liu, Q. He, Y. Meng, L. Cao, Y.-P. Sun, J. Chen and F. Lu, *Nanoscale*, 2016, **8**, 4260–4266.
26 H. Jiang, Z. Wang, H. Geng, X. Song, H. Zeng and C. Zhi, *ACS Appl. Mater. Interfaces*, 2017, **9**, 10078–10084.
27 F. Lu, C. Liu, Z. Chen, U. Veerabagu, Z. Chen, M. Liu, L. Hu, H. Xia, L. Cha and W. Zhang, *Surf. Coat. Technol.*, 2021, **420**, 127273.
28 S. Xue, Y. Wu, M. Guo, D. Liu, T. Zhang and W. Lei, *Nanoscale Res. Lett.*, 2018, **13**, 393.
29 Z. Q. Duan, M. Zhong, F. K. Shi and X. M. Xie, *Chin. Chem. Lett.*, 2016, **27**, 1490–1494.
30 S. Awasthi, J. K. Gaur and M. S. Bobji, *J. Alloys Compd.*, 2020, **848**, 156259–156269.
31 A. Haider and I.-K. Kang, *Adv. Mater. Sci. Eng.*, 2015, **2015**, 1–16.
32 L. Jing, H. Li, R. Y. Tay, B. Sun, S. H. Tsang, O. Cometto, J. Lin, E. H. T. Teo and A. I. Y. Tok, *ACS Nano*, 2017, **11**, 3742–3751.
33 W. Yin, D.-H. Lee, J. Choi, C. Park and S. M. Cho, *Korean J. Chem. Eng.*, 2008, **25**, 1358–1361.
34 L. Jing, H. Li, R. Y. Tay, B. Sun, S. H. Tsang, O. Cometto, J. Lin, E. H. T. Teo and A. I. Y. Tok, *ACS Nano*, 2017, **11**, 3742–3751.
35 J. Huang, M. Voigt, S. Wackenrohr, C. Ebbert, A. Keller, H. J. Maier and G. Grundmeier, *Mater. Corros.*, 2022, **73**, 1034–1044.
36 T. Ichibouji, T. Miyazaki, E. Ishida, A. Sugino and C. Ohtsuki, *Mater. Sci. Eng., C*, 2009, **29**, 1765–1769.
37 M. J. Frisch, G. W. Trucks, H. B. Schlegel, G. E. Scuseria, M. A. Robb, J. R. Cheeseman, G. Scalmani, V. Barone, B. Mennucci, G. A. Petersson, H. Nakatsuji, M. Caricato, X. Li, H. P. Hratchian, A. F. Izmaylov, J. Bloino, G. Zheng, J. L. Sonnenberg, M. Hada, M. Ehara, K. Toyota, R. Fukuda, J. Hasegawa, M. Ishida, T. Nakajima, Y. Honda, O. Kitao, H. Nakai, T. Vreven, J. A. Montgomery, Jr., J. E. Peralta, F. Ogliaro, M. Bearpark, J. J. Heyd, E. Brothers, K. N. Kudin, V. N. Staroverov, R. Kobayashi, J. Normand, K. Raghavachari, A. Rendell, J. C. Burant, S. S. Iyengar, J. Tomasi, M. Cossi, N. Rega, J. M. Millam, M. Klene, J. E. Knox, J. B. Cross, V. Bakken, C. Adamo, J. Jaramillo, R. Gomperts, R. E. Stratmann, O. Yazyev, A. J. Austin, R. Cammi, C. Pomelli, J. W. Ochterski, R. L. Martin, K. Morokuma, V. G. Zakrzewski, G. A. Voth, P. Salvador, J. J. Dannenberg, S. Dapprich, A. D. Daniels, Ö. Farkas, J. B. Foresman, J. V. Ortiz, J. Cioslowski, and D. J. Fox, Gaussian, Inc., Wallingford CT, 2009.
38 R. Ditchfield, W. J. Hehre and J. A. Pople, *J. Chem. Phys.*, 1971, **54**, 72.
39 C. Lee, W. Yang and R. G. Parr, *Phys. Rev. B:Condens. Matter Mater. Phys.*, 1988, **37**, 785.
40 E. R. Johnson, S. Keinan, P. Mori-Sánchez, J. Contreras-García, A. J. Cohen and W. Yang, *J. Am. Chem. Soc.*, 2010, **132**, 6498–6506.
41 J. Contreras-García, E. R. Johnson, S. Keinan, R. Chaudret, J. P. Piquemal, D. N. Beratan and W. N. Yang, *J. Chem. Theory Comput.*, 2011, **7**, 625–632.
42 L. Xing, C. Hu, Y. Zhang, X. Wang, L. Shi and R. Ran, *J. Mater. Sci.*, 2019, **54**, 3368–3382.
43 O. Nadtoka, N. Kutsevol, A. Naumenko and P. Virych, *Res. Chem. Intermed.*, 2019, **45**, 4069–4080.
44 R. Prabhakar and D. Kumar, *Polym. – Plast. Technol. Eng.*, 2016, **55**, 46–53.
45 H. M. Ibrahim, S. Zaghloul, M. Hashem and A. El-Shafei, *Cellulose*, 2021, **28**, 549–564.
46 M. Chen, L. Y. Wang, J. T. Han, J. Y. Zhang, Z. Y. Li and D. J. Qian, *J. Phys. Chem. B*, 2006, **110**, 11224–11231.
47 J. Balavijayalakshmi and V. Ramalakshmi, *J. Appl. Res. Technol.*, 2017, **15**, 413–422.
48 M. C. Ruiz-Cañas, H. I. Quintero, L. M. Corredor, E. Manrique and A. R. R. Bohórquez, *Polymers*, 2020, **12**, 5–9.

49 M. Onyszko, A. Markowska-Szczupak, R. Rakoczy, O. Paszkiewicz, J. Janusz, A. Gorgon-Kuza, K. Wenelska and E. Mijowska, *Int. J. Mol. Sci.*, 2020, **21**, 1–15.
50 S. Awasthi, S. K. Pandey, J. K. Gaur and C. Srivastava, *Mater. Chem. Front.*, 2022, **6**, 3731–3747.
51 S. Sivaselvam, R. Selvakumar, C. Viswanathan and N. Ponpandian, *Chemosphere*.
52 K. Prusty, A. Biswal, S. B. Biswal and S. K. Swain, *Mater. Chem. Phys.*, 2019, **234**, 378–389.
53 S. Saber-Samandari and M. Gazi, *J. Taiwan Inst. Chem. Eng.*, 2015, **51**, 143–151.
54 X. Hu, R. Liang, J. Li, Z. Liu and G. Sun, *Mater. Des.*, 2019, **163**, 107547.
55 Y. L. Luo, C. H. Zhang, Y. S. Chen and W. Yang, *Mater. Res. Innovations*, 2009, **13**, 18–27.
56 X. Gao, T. Deng, X. Huang, M. Yu, D. Li, J. Lin, C. Yu, C. Tang and Y. Huang, *Soft Matter*, 2022, **18**, 859–866.
57 E. K. Sam, D. K. Sam, J. Chen, X. Lv and J. Liu, *J. Porous Mater.*, 2020, **27**, 1149–1158.
58 H. U. Rehman, Y. Chen, Y. Guo, Q. Du, J. Zhou, Y. Guo, H. Duan, H. Li and H. Liu, *Composites, Part A*, 2016, **90**, 250–260.
59 C. Eriksson, H. Nygren and K. Ohlson, *Biomaterials*, 2004, **25**, 4759–4766.
60 Z. Jia, P. Xiu and M. Li, *Biomaterials*, 2016, **75**, 203–222.
61 R. S. Cataliotti, F. Aliotta and R. Ponterio, *Phys. Chem. Chem. Phys.*, 2009, **11**, 11258–11263.
62 A. Boukheit, F. Chabert, B. Otazaghine and A. Taguet, *Nanomaterials*, 2022, **12**, 2735.
63 E. Sharmin, M. T. Kafyah, A. A. Alzaydi, A. A. Fatani, F. A. Hazazzi, S. K. Babgi, N. M. Alqarhi, A. A. H. Sindi, D. Akram, M. Alam, J. Alam, L. A. Al-Madboly, N. A. Shoeib, A. M. Alqahtani and M. Mojally, *Int. J. Biol. Macromol.*, 2020, **163**, 2236–2247.
64 X. Gao, T. Deng, X. Huang, M. Yu, D. Li, J. Lin, C. Yu, C. Tang and Y. Huang, *Soft Matter*, 2022, **18**, 859–866.
65 G. Di Luca, G. Chen, W. Jin and A. Gugliuzza, *Membranes*, 2023, **13**, 437.
66 X. Wang, H. Hou, Y. Li, Y. Wang, C. Hao and C. Ge, *J. Ind. Eng. Chem.*, 2016, **41**, 82–90.
67 C. Ferrag, S. Li, K. Jeon, N. M. Andoy, R. M. A. Sullan, S. Mikhaylichenko and K. Kerman, *Colloids Surf., B*, 2021, **197**, 111397.
68 S. Butylina, S. Geng and K. Oksman, *Eur. Polym. J.*, 2016, **81**, 386–396.
69 S. Awasthi, S. K. Pandey, A. Juyal, C. P. Pandey and K. Balani, *J. Alloys Compd.*, 2017, **711**, 424–433.
70 S. Awasthi, S. K. Pandey, E. Arunan and C. Srivastava, *J. Mater. Chem. B*, 2021, **9**, 228–249.
71 C. Khurana, P. Sharma, O. P. Pandey and B. Chudasama, *J. Mater. Sci. Technol.*, 2016, **32**, 524–532.
72 G. Sharma, Z. A. Alothman, A. Kumar, S. Sharma, S. K. Ponnusamy and Mu. Naushad, *Nanotechnol. Environ. Eng.*, 2017, **2**, 4.
73 K. Y. Gudz, L. Yu. Antipina, E. S. Permyakova, A. M. Kovalskii, A. S. Konopatsky, S. Yu. Filippovich, I. A. Dyatlov, P. V. Slukin, S. G. Ignatov and D. V. Shtansky, *ACS Appl. Mater. Interfaces*, 2021, **13**, 23452–23468.
74 D. Cremer and E. Kraka, *Croat. Chem. Acta, CCA*, 1984, **57**, 1259–1281.
75 R. Singh, K. Singh and S. K. Pandey, *ChemistrySelect*, 2018, **3**, 13048–13056.
76 E. Scrocco and J. Tomasi, *Adv. Quantum Chem.*, 1978, **11**, 115–121.